



Time-varying hydrodynamics of a flexible riser under multi-frequency vortex-induced vibrations



Chang Liu ^{a,b,c}, Shixiao Fu ^{a,b,*}, Mengmeng Zhang ^{a,b}, Haojie Ren ^{a,b}

^a State Key Laboratory of Ocean Engineering, Shanghai Jiao Tong University, Shanghai 200240, China

^b Collaborative Innovation Centre for Advanced Ship and Deep-Sea Exploration, Shanghai 200240, China

^c Department of Mechanical Engineering, Johns Hopkins University, Baltimore, MD 21218, USA

ARTICLE INFO

Article history:

Received 20 April 2017

Received in revised form 8 February 2018

Accepted 14 March 2018

Available online 10 May 2018

Keywords:

Vortex-induced vibration

Vortex-induced force coefficients

Time-varying hydrodynamics

Forgetting factor least squares method

ABSTRACT

This paper proposes the Forgetting Factor Least Squares (FF-LS) method for identification of time-varying hydrodynamics of a flexible riser under multi-frequency vortex-induced vibrations (VIV). Differing from the traditional least squares method used to identify hydrodynamics, with equal weights on all sampled data, this method introduces a forgetting factor to give higher weight to data closer to the present moment. FF-LS allows the possibility of handling the time-varying parameters. By following this procedure for all sampled data of a flexible riser undergoing multi-frequency VIV, the corresponding time-varying hydrodynamics in the Cross-Flow (CF) direction will be obtained considering multi-frequency coupling. The results show that, under multi-frequency coupling, vortex-induced force coefficients of flexible risers change periodically and differ from coefficients at the basic frequency usually used in VIV prediction. This difference is a result of the coupling effect between the basic frequency and high frequency. Time-varying coefficients considering multi-frequency coupling contain steady components and vibration components whose frequencies are the sum of coupling frequencies and the difference of coupling frequencies. To show the advantages of time-varying hydrodynamics, we compare forces reconstructed from different vortex-induced force coefficients, assuming vortex-induced force obtained from the inverse analysis is the real force. The results show that time-varying vortex-induced force coefficients considering a coupling effect between multiple frequencies can accurately reconstruct vortex-induced force, while the sum of vortex-induced force coefficients under multiple frequencies will produce the cross-term that overestimates the vortex-induced force.

© 2018 Elsevier Ltd. All rights reserved.

1. Introduction

When predicting vortex-induced vibration (VIV) of a flexible riser, the construction of the vortex-induced force directly determines the accuracy of the VIV prediction results. The existing semi-empirical prediction models for VIV are based on the vortex-induced force coefficients database obtained from the one degree of freedom forced oscillation test of the rigid cylinder (pure CF or pure IL) (Gopalkrishnan, 1993; Larsen et al., 2007). The vortex-induced force coefficients database includes the excitation coefficient and added-mass coefficient.

In the real case, VIV exists in the in-line (IL) direction and cross-flow (CF) direction, and VIV in these two directions is strongly coupled. This coupling introduces strong coupling of hydrodynamics in the two directions as well. Through a low

* Corresponding author at: State Key Laboratory of Ocean Engineering, Shanghai Jiao Tong University, Shanghai 200240, China.

E-mail address: shixiao.fu@sjtu.edu.cn (S. Fu).

mass-ratio two-dimensional free vibration experiment, Jauvtis and Williamson (2004) revealed the characteristics of VIV responses considering the coupling effect of the CF direction and IL direction. Differing from the VIV in the one-dimensional free vibration test, the 2T vortex shedding mode (a triplet of vortices being formed in each half cycle) in the wake vortex was observed. Dahl et al. (2007) further states that multi vortex patterns are the primary contributor for the high-frequency (third-order) component in the lift force. To obtain a database of VIV that more accurately predicts the VIV response in the CF direction of the riser, Dahl (2008) carried out the two-dimensional forced oscillations of rigid cylinders which provided the hydrodynamics coefficient database for the calculation of vortex-induced force, especially the third-order high-frequency forces. However, the database is relatively sparse, and the accuracy of the vortex-induced vibration predictions based on this database has not yet been validated.

The rigid cylinder forced oscillation test conveniently establishes a hydrodynamic coefficient database for vortex-induced vibration predictions, but the flexible riser differs from a rigid cylinder because of the coupling effect of the CF and IL direction and the three-dimensional flow field effect (Marcollo and Hinwood, 2006; Sumer and Fredsøe, 2006). For the flexible riser scaled model test, Vandiver et al. (2009, 2006) found a high-order response at three times the basic frequency in the CF direction and four times the basic frequency in the IL direction, which indicates high-frequency vortex-induced force exists in a real flexible riser. This high-frequency force causes high-frequency VIV response. Hu et al. (2014) also found the high-order response in laboratory experimental VIV signals from the Norwegian Deepwater Program (NDP) high mode test (Trim et al., 2005). Furthermore, Zheng et al. (2014) found that by including third-order higher harmonic components, there is a fatigue damage increase of up to 50% compared with the damage due to the first-order harmonic stress only and the fatigue damage increases by another 20% due to a wide-spread Power Spectrum Density (PSD). Using buoyancy elements and strakes also cause multiple lock-in frequencies to compete with each other (Fang et al., 2014; Li et al., 2013, 2011; Lie et al., 1998). Wu et al. (2016) obtained the vortex-induced force and its coefficients at the lock-in frequency in the CF direction of a riser using the beam finite element equation and the inverse analysis based on the optimal control theory. Focusing on the lock-in frequency, Song et al. (2016) used the method of modal analysis combined with the Euler beam dynamic response equation to analyze hydrodynamic force. Strain information measured from a flexible riser scaled model test is used to obtain the hydrodynamic characteristics at the lock-in frequency. For the vortex-induced force and VIV response at a single frequency, the hydrodynamic load is decomposed into excitation force in phase with the velocity and added-mass force in phase with the acceleration. These two force components are normalized to the excitation coefficient and the added-mass coefficient, respectively. Vortex-induced force coefficients obtained at a single frequency can be used to accurately reconstruct the hydrodynamic force at a specific frequency.

However, hydrodynamic characteristics of a flexible riser under the multi-frequency coupling are not considered in the papers mentioned above because effective analysis methods are not available. Using only vortex-induced force coefficients under a single frequency cannot accurately reconstruct the real vortex-induced force or predict the multi-frequency VIV precisely either.

This paper proposes the Forgetting Factor Least Squares Method (FF-LS) for identification of time-varying hydrodynamics of a flexible riser under multi-frequency vortex-induced vibrations (VIV). Differing from the traditional least squares method used to identify hydrodynamics (Song et al., 2016) with equal weights on all sampled data, this approach introduces a forgetting factor to give higher weight to data closer to the present moment (Section 2). FF-LS allows the possibility of handling time-varying parameters. By following this procedure for all sampled data of a flexible riser undergoing multi-frequency VIV (Section 3), the corresponding time-varying hydrodynamics considering multi-frequency coupling is obtained. Characteristics of time-varying vortex-induced force coefficients under multi-frequency coupling are also analyzed.

2. Time-varying hydrodynamics identification

2.1. Time-varying hydrodynamics identification method

When flexible risers undergo vortex-induced vibration, the frequency where the power spectral density of the VIV response in the CF direction reaches maximum value is regarded as the basic frequency (henceforth, all basic frequency is thus defined). Vibration in the CF direction usually consists of multi-frequency vibrations that are odd times of the basic frequency ω , 3ω , 5ω . . . , while vibration in the IL direction consists of multi-frequency vibrations that are even times of the basic frequency 2ω , 4ω , 6ω The vibrations that are three times or more of the basic frequency in the CF direction and four times or more in the IL direction are called high-frequency response (Vandiver et al., 2009). Recently, more complicated characteristics such as chaotic type motions are observed in the vortex-induced vibration of the long riser (Li et al., 2011; Zheng et al., 2014). Therefore, this paper considers more general cases, where we express displacement response time history of the riser in the CF and IL directions as follows:

$$\begin{aligned} y(z, t) &= \sum_i y(z, t, \omega_i) \quad i = 1, 2, 3 \dots \\ x(z, t) &= x_0(z) + \sum_i x(z, t, \omega_i) \quad i = 1, 2, 3 \dots \end{aligned} \tag{1}$$

In the above equation, z is the axial position of a flexible riser, t denotes time, ω_i is the i th response frequency, $y(z, t, \omega_i)$ represents the time history of displacement at the position z in the CF direction at a single vibration frequency ω_i . Similarly,

$x(z, t, \omega_i)$ describes the time history of displacement at the location z in the IL direction at a single vibration frequency ω_i and $x_0(z)$ represents the time average bending movement in the IL direction.

In the following, we establish a model of time-varying vortex-induced force coefficients of a flexible riser under multi-frequency VIV. The derivation of the vortex-induced force coefficients in the IL direction is similar to that in the CF direction.

The displacement time history $y(z, t)$ in the riser CF direction at node z is described as a linear superposition of several single frequency responses:

$$y(z, t) = \sum_i y(z, t, \omega_i) = \sum_i y_0(z, \omega_i) \sin(\omega_i t + \varphi_i) \quad i = 1, 2, 3 \dots \quad (2)$$

where ω_i is the i th circular response frequency component of the VIV response in the CF direction; $y_0(z, \omega_i)$ is the displacement amplitude of the frequency ω_i ; φ_i is the initial phase angle at frequency ω_i , which do not change over time. The VIV velocity and acceleration time history at node z can be obtained by differentiating the VIV displacement:

$$\begin{aligned} \dot{y}(z, t) &= \sum_i \dot{y}(z, t, \omega_i) = \sum_i \omega_i y_0(z, \omega_i) \cos(\omega_i t + \varphi_i) \\ \ddot{y}(z, t) &= \sum_i \ddot{y}(z, t, \omega_i) = -\sum_i \omega_i^2 y_0(z, \omega_i) \sin(\omega_i t + \varphi_i) \quad i = 1, 2, 3 \dots \end{aligned} \quad (3)$$

In this case, the time history of vortex-induced force in the CF direction at node z is:

$$f_{CF}(z, t) = \sum_i f(z, t, \omega_i) = \sum_i f_0(z, \omega_i) \sin(\omega_i t + \varphi_i + \theta_i) \quad (4)$$

where $f(z, t, \omega_i)$ is the vortex-induced force at frequency ω_i , $f_0(z, \omega_i)$ is the amplitude of vortex-induced force at frequency ω_i , θ_i is the initial phase difference between force and VIV displacement at ω_i , which also do not change over time.

The equation above can be expanded to:

$$\begin{aligned} f_{CF}(z, t) &= \sum_i f_{CF}(z, t, \omega_i) \\ &= \sum_i f_0(z, \omega_i) \sin \theta_i \cos(\omega_i t + \varphi_i) - \left[-\sum_i f_0(z, \omega_i) \cos \theta_i \sin(\omega_i t + \varphi_i) \right] \end{aligned} \quad (5)$$

where $f_0(z, \omega_i) \sin \theta_i \cos(\omega_i t + \varphi_i)$ is part of the vortex-induced force in phase with velocity $\dot{y}(z, t, \omega_i)$ at the corresponding frequency, namely, excitation force:

$$f_0(z, \omega_i) \sin \theta_i \cos(\omega_i t + \varphi_i) = \frac{\rho D l}{2\sqrt{2}\dot{y}_{RMS}(z, \omega_i)} U^2(z, t) CLe(z, \omega_i) \dot{y}(z, t, \omega_i). \quad (6)$$

In the above equation, l is the element unit length; $CLe(z, \omega_i)$ is the excitation coefficient at the node z at the frequency ω_i ; ρ is the fluid density; $U(z, t)$ is flow velocity relative to the riser (VIV velocity of the riser not included) at node z at t moment; D is the hydrodynamic diameter of the riser. $\dot{y}_{RMS}(z, \omega_i)$ is the Root Mean Square (RMS) value of VIV velocity for node z at frequency ω_i :

$$\dot{y}_{RMS}(z, \omega_i) = \sqrt{\frac{1}{T} \int_0^T \dot{y}(z, t, \omega_i)^2 dt}. \quad (7)$$

When the vortex-induced vibration of the riser is a single frequency harmonic response, $\sqrt{2}\dot{y}_{RMS}(z, \omega_i)$ is equal to the amplitude of the VIV velocity:

$$\sqrt{2}\dot{y}_{RMS}(z, \omega_i) = \dot{y}_0(z, \omega_i). \quad (8)$$

The formula above is only valid for a single frequency harmonic response, the RMS value of VIV velocity for multi-frequency response is derived below.

The term $-f_0(z, \omega_i) \cos \theta_i \sin(\omega_i t + \varphi_i)$ in Eq. (5) is the part of the vortex-induced force in phase with acceleration $\ddot{y}(z, t)$; namely, added-mass force, which can be expressed as:

$$-f_0(z, \omega_i) \cos \theta_i \sin(\omega_i t + \varphi_i) = \frac{1}{4} \rho \pi D^2 l CLa(z, \omega_i) \ddot{y}(z, t, \omega_i). \quad (9)$$

In the equation above, $CLa(z, \omega_i)$ is the added-mass coefficient at node z at frequency ω_i .

Substituting Eqs. (6) and (9) into Eq. (5), we get:

$$\begin{aligned} f_{CF}(z, t) &= \sum_i f_{CF}(z, t, \omega_i) \\ &= \sum_i \left[\frac{\rho D l U^2(z, t)}{2\sqrt{2}\dot{y}_{RMS}(z, \omega_i)} CLe(z, \omega_i) \dot{y}(z, t, \omega_i) - \frac{\rho \pi D^2 l}{4} CLa(z, \omega_i) \ddot{y}(z, t, \omega_i) \right]. \end{aligned} \quad (10)$$

In this equation, $CLe(z, \omega_i)$ and $CLA(z, \omega_i)$ are excitation coefficient and added-mass coefficient at node z at frequency ω_i in the CF direction.

To consider the coupling effect between multiple frequencies, we build the time-varying hydrodynamic coefficients model. Similarly, Wiggins (2005) also used time-varying hydrodynamic coefficients to consider multi-frequency coupling. Rewrite Eq. (10) as below:

$$f_{CF}(z, t) = \frac{\rho D l U^2(z, t)}{2\sqrt{2}\dot{y}_{RMS}(z)} CLe(z, t)\dot{y}(z, t) - \frac{\rho \pi D^2 l}{4} CLA(z, t)\ddot{y}(z, t) \quad (11)$$

where

$$\begin{cases} \dot{y}(z, t) = \sum_i \dot{y}(z, t, \omega_i) & i = 1, 2, 3, \dots \\ \ddot{y}(z, t) = \sum_i \ddot{y}(z, t, \omega_i) & i = 1, 2, 3, \dots \\ f_{CF}(z, t) = \sum_i f_{CF}(z, t, \omega_i) & i = 1, 2, 3, \dots \\ \dot{y}_{RMS}(z) = RMS(\sum_i \dot{y}(z, t, \omega_i)) & i = 1, 2, 3, \dots \end{cases} \quad (12)$$

represents the linear superposition of several velocities, accelerations, vortex-induced forces, and RMS value of velocity superposition under multiple frequencies.

For multi-frequency cases, the RMS value of velocity is defined as:

$$\dot{y}_{RMS}(z) = RMS(\sum_i \dot{y}(z, t, \omega_i)) = \sqrt{\frac{1}{T} \int_0^T [\sum_i \dot{y}(z, t, \omega_i)]^2 dt} \quad (13)$$

where T is the least common multiple of different vibration period. Specifically, if $\omega_i = (2*i - 1)*\omega_1$, $i = 1, 2, 3, \dots$, T is equal to $\frac{2\pi}{\omega_1}$. The RMS value of multiple frequencies is:

$$\begin{aligned} RMS(\sum_i \dot{y}(z, t, \omega_i)) &= \sqrt{\frac{1}{T} \int_0^T [\sum_i \dot{y}(z, t, \omega_i)]^2 dt} \\ &= \sqrt{\frac{1}{T} \int_0^T \left[\sum_i \dot{y}(z, t, \omega_i)^2 + \sum_i \sum_{i \neq j} \dot{y}(z, t, \omega_i) \dot{y}(z, t, \omega_j) \right] dt}. \end{aligned} \quad (14)$$

Considering the trigonometric function set $\{\cos n\omega_1 t, \sin n\omega_1 t\} (n = 0, 1, 2, \dots, \infty)$ constitutes a complete orthogonal function set in the interval $(t_0, t_0 + T_1)$, $T_1 = \frac{2\pi}{\omega_1}$; i.e.,

$$\begin{aligned} \int_{t_0}^{t_0+T_1} \cos m\omega_1 t \cos n\omega_1 t dt &= 0 (m \neq n) \\ \int_{t_0}^{t_0+T_1} \sin m\omega_1 t \sin n\omega_1 t dt &= 0 (m \neq n) \\ \int_{t_0}^{t_0+T_1} \cos m\omega_1 t \sin n\omega_1 t dt &= 0, \end{aligned} \quad (15)$$

we substitute $\dot{y}(z, t, \omega_i) = \omega_i y_0(z, \omega_i) \cos(\omega_i t + \varphi_i)$ in Eq. (3) into the RMS value calculation, to get:

$$RMS(\sum_i \dot{y}(z, t, \omega_i)) = \sqrt{\sum_i \frac{1}{T} \int_0^T \dot{y}(z, t, \omega_i)^2 dt} = \sqrt{\sum_i \dot{y}_{RMS}(z, \omega_i)^2}. \quad (16)$$

In Eq. (11) $CLe(z, t)$, $CLA(z, t)$ are the time-varying excitation coefficient and added-mass coefficient, which replace the vortex-induced force coefficients at multiple frequencies $CLe_i(z, \omega_i)$, $CLA_i(z, \omega_i)$ $i = 1, 2, 3, \dots$ in Eq. (10). Time-varying vortex-induced force coefficients $CLe(z, t)$, $CLA(z, t)$ consider the vortex-induced force coefficients at multiple frequencies and the coupling effect at different frequencies.

When the above summing symbols contain only a single frequency response or force, the obtained coefficients $CLe(z, t)$, $CLA(z, t)$ do not change over time (Liu et al., 2017), and the definition of hydrodynamic coefficients are consistent with the hydrodynamic coefficients defined by Song et al. (2016) and Gopalkrishnan (1993).

Then the **Forgetting Factor Least Squares method** (FF-LS) (Ding and Chen, 2005; Paleologu et al., 2008) is introduced to identify the time-varying vortex-induced force coefficients in Eq. (11). This method introduces a forgetting factor, which divides the time history of the sampling data into different regions and gives higher weight to data closer to the present moment. This modification improves the sensitivity of the Least Squares method and makes it possible to identify the time-varying parameters under multi-frequency coupling accurately.

For the time-varying hydrodynamics identification problem in Eq. (11), time history of force, response and time-varying coefficients can be expressed in matrix form:

$$\begin{aligned}\mathbf{f}_L &= [f_{CF}(z, t_1), f_{CF}(z, t_2), f_{CF}(z, t_3), \dots, f_{CF}(z, t_L)]^T \\ \mathbf{H}_L &= [\mathbf{h}(1), \mathbf{h}(2), \mathbf{h}(3), \dots, \mathbf{h}(L)]^T \\ &= \left[\begin{array}{c} \dot{y}(z, t_1), \dot{y}(z, t_2), \dot{y}(z, t_3), \dots, \dot{y}(z, t_L) \\ \ddot{y}(z, t_1), \ddot{y}(z, t_2), \ddot{y}(z, t_3), \dots, \ddot{y}(z, t_L) \end{array} \right]^T \\ \boldsymbol{\theta}(L) &= \left[\begin{array}{c} \frac{\rho D U^2}{2\sqrt{2}\dot{y}_{RMS}(z)} CLe(z, t_L) \\ -\frac{\rho \pi D^2}{4} CLa(z, t_L) \end{array} \right] \\ L &= 1, 2, 3, \dots\end{aligned}\tag{17}$$

In the equation above, the initial moment and present moment are denoted as t_1 and t_L , respectively. $t_1, t_2, t_3, \dots, t_L$ represent sampling time, and L groups of data are sampled in total. z represents the spatial position of the data, and the rows of the above three matrices represent the values at different sampling moments. \mathbf{f}_L is the time history vortex-induced force at node z from the initial moment t_1 to the present moment t_L . \mathbf{H}_L is the time history of velocity and acceleration at node z from the initial moment t_1 to the present moment t_L and $\boldsymbol{\theta}(L)$ is dimensional vortex-induced force coefficient at node z at moment t_L .

Identification of time-varying hydrodynamics can be written as identifying the time history of a set of parameters $\boldsymbol{\theta}(L)$ $L = 1, 2, 3, \dots$, which satisfies:

$$\mathbf{f}_L = \mathbf{H}_L \boldsymbol{\theta}(L) \quad L = 1, 2, 3, \dots\tag{18}$$

Eq. (18) utilizes all previous historical moments data before t_L to identify time-varying parameter $\boldsymbol{\theta}(L)$.

Then, the sampled force and response are multiplied at different moments by different data weights. The data weight is larger if the data is closer to the present moment t_L . Specifically, the data weight of the present moment is $\beta^0 = 1$, the data weight of the initial moment is β^{L-1} (β is a constant, which satisfies $0 < \beta \leq 1$). The force with data weight multiplied is:

$$\mathbf{f}_L^* = [\beta^{L-1} \mathbf{f}_L(1), \beta^{L-2} \mathbf{f}_L(2), \dots, \beta \mathbf{f}_L(L-1), \mathbf{f}_L(L)]^T.\tag{19}$$

The same weighting process is applied to the sampled response:

$$\mathbf{H}_L^* = [\beta^{L-1} \mathbf{h}^T(1), \beta^{L-2} \mathbf{h}^T(2), \dots, \beta \mathbf{h}^T(L-1), \mathbf{h}^T(L)]^T.\tag{20}$$

Therefore, the solution model is rewritten as follows:

$$\mathbf{f}_L^* = \mathbf{H}_L^* \boldsymbol{\theta}(L).\tag{21}$$

According to the basic principle of the Least Squares method (Chavent, 1979), the parameters to be identified need to minimize the sum squared errors between $\mathbf{H}_L^* \boldsymbol{\theta}(L)$ and \mathbf{f}_L^* ; namely:

$$\min J(\boldsymbol{\theta}(L)) = (\mathbf{f}_L^* - \mathbf{H}_L^* \boldsymbol{\theta}(L))^T (\mathbf{f}_L^* - \mathbf{H}_L^* \boldsymbol{\theta}(L)).\tag{22}$$

Assuming that $\hat{\boldsymbol{\theta}}(L)$ satisfies $J(\boldsymbol{\theta}(L))|_{\hat{\boldsymbol{\theta}}(L)} = \min$, there is

$$\frac{\partial J(\boldsymbol{\theta}(L))}{\partial \boldsymbol{\theta}(L)} \Big|_{\boldsymbol{\theta}(L)=\hat{\boldsymbol{\theta}}(L)} = \frac{\partial}{\partial \boldsymbol{\theta}(L)} (\mathbf{f}_L^* - \mathbf{H}_L^* \boldsymbol{\theta}(L))^T (\mathbf{f}_L^* - \mathbf{H}_L^* \boldsymbol{\theta}(L)) \Big|_{\boldsymbol{\theta}(L)=\hat{\boldsymbol{\theta}}(L)} = \mathbf{0}^T.\tag{23}$$

Expanding this equation and using the following two vector differential formula:

$$\begin{cases} \frac{\partial}{\partial \mathbf{x}} (\mathbf{a}^T \mathbf{x}) = \mathbf{a}^T \\ \frac{\partial}{\partial \mathbf{x}} (\mathbf{x}^T \mathbf{A} \mathbf{x}) = 2\mathbf{x}^T \mathbf{A}. \end{cases}\tag{24}$$

Eq. (23) becomes:

$$(\mathbf{H}_L^*{}^T \mathbf{H}_L^*) \hat{\boldsymbol{\theta}}(L) = \mathbf{H}_L^*{}^T \mathbf{f}_L^*.\tag{25}$$

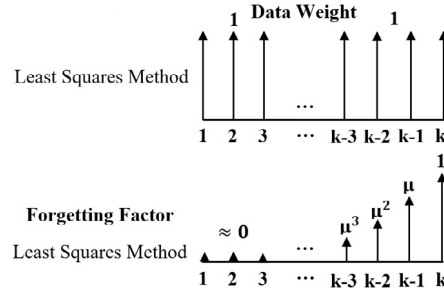


Fig. 1. Schematic of data weight for forgetting factor least square method.

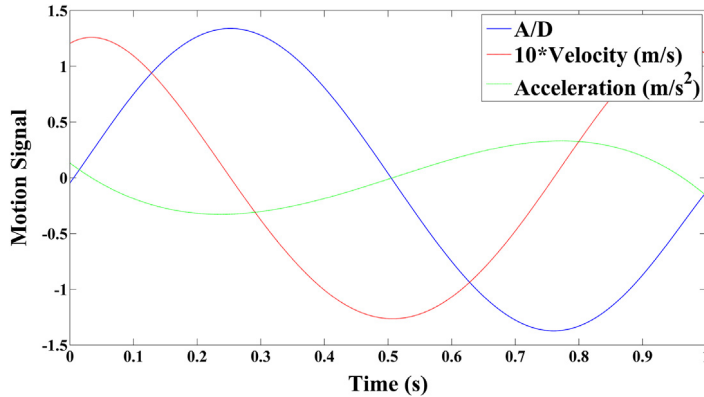


Fig. 2. Motion signal from Jauvtis and Williamson (2004) when the 2T mode vortex appears.

The equation above is called the regular equation. When $\mathbf{H}_L^{*T} \mathbf{H}_L^*$ is a non-singular matrix, we obtain:

$$\hat{\theta}(L) = (\mathbf{H}_L^{*T} \mathbf{H}_L^*)^{-1} \mathbf{H}_L^{*T} \mathbf{f}_L^*. \quad (26)$$

Substituting Eqs. (19) and (20) into Eq. (26), we obtain:

$$\begin{aligned} \hat{\theta}(L) &= \left[\sum_{i=1}^L \beta^{2(L-i)} \mathbf{h}(i) \mathbf{h}^T(i) \right]^{-1} \left[\sum_{i=1}^L \beta^{2(L-i)} \mathbf{h}(i) f_{CF}(z, t_i) \right] \\ &= \left[\sum_{i=1}^L \mu^{(L-i)} \mathbf{h}(i) \mathbf{h}^T(i) \right]^{-1} \left[\sum_{i=1}^L \mu^{(L-i)} \mathbf{h}(i) f_{CF}(z, t_i) \right] \\ &= (\mathbf{H}_L^T \Lambda_L \mathbf{H}_L)^{-1} \mathbf{H}_L^T \Lambda_L \mathbf{f}_L \end{aligned} \quad (27)$$

where $\mu = \beta^2$, $0 < \mu \leq 1$. μ is called the **Forgetting Factor**. Λ_L is the weighted matrix, whose diagonal elements are $\Lambda(L) = 1$ and $\Lambda(k-1) = \mu \Lambda(k)$ and off-diagonal elements are 0. The essence of this method is to give different weights to the data; the further from the present moment of data: the smaller the weight, as shown in Fig. 1.

Verification of the proposed method for identifying time-varying parameters and hydrodynamic coefficients of the flexible riser is presented in the next sub-section and Appendix A, respectively. In Section 3, we apply this method to experimental data of a flexible riser (Section 3.1), where VIV response is obtained through modal analysis, and vortex-induced force is obtained through the inverse analysis method (Section 3.2). Primary results of obtained time-varying vortex-induced force coefficients are shown in Section 3.3.

2.2. Validation of identification method

Initially, we verify the proposed FF-LS method using motion signals (Fig. 2) and force signals (called real force) from a two-dimensional free vibration test (Figure 18(b) in Jauvtis and Williamson, 2004). In this case, the 2T mode vortex appears, and the lift force consists of multi-frequency components.

To render the analogy between validation in Section 2.2 and the hydrodynamics identification problem more understandable, we use similar symbols. For the rigid cylinder test and the mass–spring–dashpot system, contrasting the symbols used

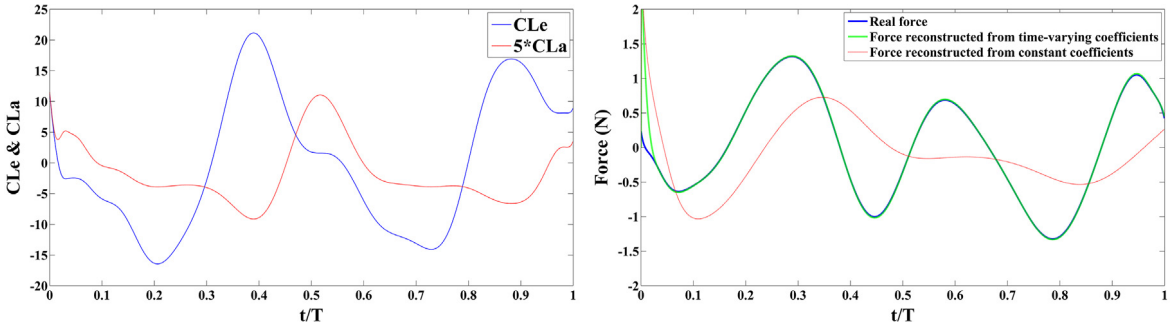


Fig. 3. Identified time-varying coefficients (left) and comparison (left) of real force, force reconstructed from time-varying coefficients, and force reconstructed from constant coefficients.

Table 1

Parameters of an elastically mounted rigid cylinder under uniform flow.

Parameters	Value	Parameters	Value
Mass of cylinder m (kg)	3.7486	Mass ratio m^* = $\frac{m}{\pi \rho D^2 L/4}$	8.63
Damping c (kg/s)	0.07132	Natural frequency $f_N = \frac{1}{2\pi} \sqrt{\frac{k}{m}} (1 - \xi^2)$ Hz	1
Stiffness k (N/m)	147.989	Damping ratio $\xi = \frac{c}{2\sqrt{mk}}$	0.15%
Flow velocity U (m/s)	0.2667	Reduced velocity $U^* = \frac{U}{f_N D}$	7
Flow density ρ (kg/m ³)	1000	Length ratio L/D	20
Diameter of cylinder D (m)	0.0381	Amplitude ratio $A^* = A_{\max}/D$	0.6

for the flexible riser, no variables are related to the location. Similar to the vortex-induced force decomposition method of the flexible riser in Section 2.1, the real force signal can be decomposed into excitation force $F_v(t) = CLe(t) \frac{\rho U^2 D L}{2} \dot{y}(t)$ related to velocity and added-mass force $F_a(t) = CLa(t) \frac{\pi \rho D^2 L}{4} \ddot{y}(t)$ related to acceleration; namely:

$$F_{Recon}(t) = CLe(t) \frac{\rho U^2 D L}{2} \dot{y}(t) + CLa(t) \frac{\pi \rho D^2 L}{4} \ddot{y}(t). \quad (28)$$

$CLe(t)$ and $CLa(t)$ are called the excitation coefficient and added-mass coefficient, respectively, for the cylinder under free vibration. Similar to the identification of the vortex-induced force coefficient of the flexible riser, the sum of squared errors between the force signal reconstructed from the identified coefficients $F_{Recon}(t) = CLe(t) \frac{\rho U^2 D L}{2} \dot{y}(t) + CLa(t) \frac{\pi \rho D^2 L}{4} \ddot{y}(t)$ and the real force signal should be minimized:

$$\min[F_{real}(t) - F_{Recon}(t)]^2. \quad (29)$$

Namely, for any moment t_L , substituting the time history of $F_{real}(t)$ from the initial moment t_1 to the present moment t_L as \mathbf{f}_L and the time history of $\dot{y}(t)$, $\ddot{y}(t)$ from the initial moment t_1 to the present moment t_L as \mathbf{H}_L in Eq. (17), causes Eq. (27) to yield results of $\theta(L)$, which is $CLe(t)$, $CLa(t)$ at moment t_L in this case.

Fig. 3 shows the identified time-varying coefficients and comparison of real force, force reconstructed from time-varying coefficients, and force reconstructed from constant coefficients ($CLe = -0.0697$, $CLa = -0.1054$). Compared with time-varying coefficients, the constant coefficient model cannot accurately reconstruct the real force.

Furthermore, the numerical mass–spring–dashpot model is used to verify that the FF–LS method proposed in this paper can accurately identify time-varying force coefficients. Identified time-varying coefficients provide some inspiration for multi-frequency coupling effect. The following problem of an elastically mounted rigid cylinder under uniform flow is constructed, and the non-dimensional parameters (Table 1) follow that in Govardhan and Williamson (2000) to give more physical results.

The displacement is constructed as a known signal $y(t)$. Velocity and acceleration $\dot{y}(t)$, $\ddot{y}(t)$ are the first-order and second-order time derivatives of the displacement signal. According to the dynamics of the mass–spring–dashpot system, the hydrodynamic force signal (added-mass force included) $F_{real}(t)$ that causes this motion should satisfy the equation below (Williamson and Govardhan, 2004), which is denoted as the real force for the numerical mass–spring–dashpot system:

$$F_{real}(t) = m\ddot{y}(t) + c\dot{y}(t) + ky(t). \quad (30)$$

In this equation, m , c , k are mass, damping of the dashpot and stiffness of spring, respectively, and they are constant.

For single frequency signal, the identified coefficients will not vary over time, and FF–LS method gives the same results as the analytical solution (Liu et al., 2017). In this paper, we focus on two types of motion signal that will lead to time-varying

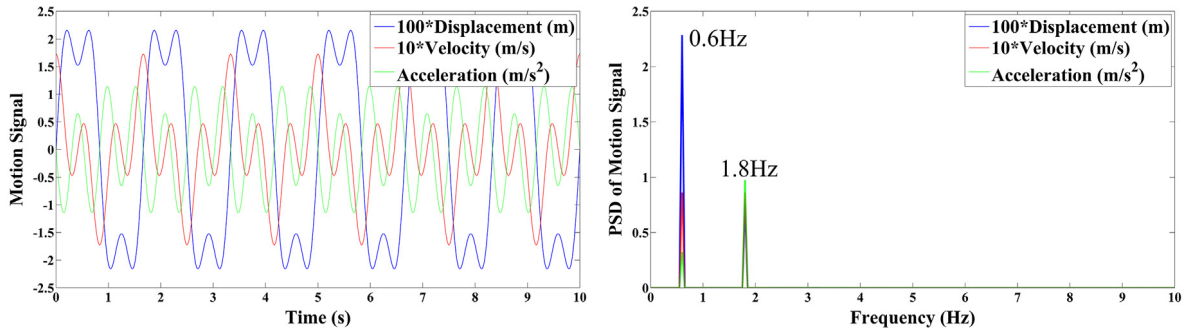


Fig. 4. Time history (left) and Power spectral density (right) of the motion superposition under ω_1 and ω_2 (displacement, velocity, and acceleration).

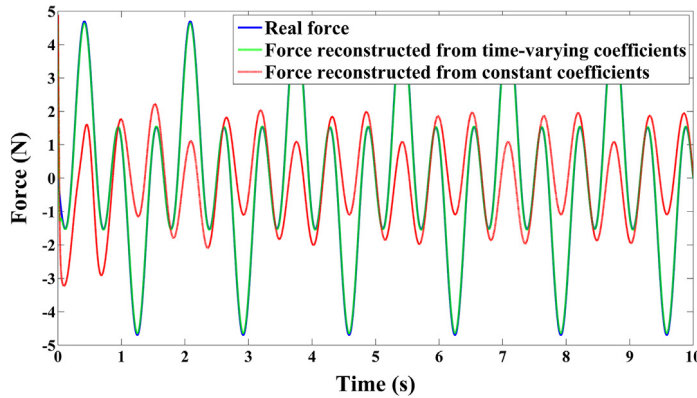


Fig. 5. Comparison of real force, force reconstructed from constant coefficients and that reconstructed from time-varying coefficient obtained by FF-LS method.

effects of identified coefficients. There are two types of motion signals: type 1 signal is the superposition of two frequency signals and type 2 signal is the superposition of the broadband frequency signals.

Type 1 motion signals are set as:

$$\begin{cases} y(t) = A_1 \sin(2\pi f_1 t + \varphi_1) + A_2 \sin(2\pi f_2 t + \varphi_2) \\ \dot{y}(t) = 2\pi f_1 A_1 \cos(2\pi f_1 t + \varphi_1) + 2\pi f_2 A_2 \cos(2\pi f_2 t + \varphi_2) \\ \ddot{y}(t) = -(2\pi f_1)^2 A_1 \sin(2\pi f_1 t + \varphi_1) - (2\pi f_2)^2 A_2 \sin(2\pi f_2 t + \varphi_2) \end{cases} \quad (31)$$

where vibration amplitudes $A_1 = 0.02286$ m, $A_2 = 0.01143$ m, vibration frequencies $f_1 = 0.6$ Hz, $f_2 = 3f_1 = 1.8$ Hz, and the initial phase angle is 0. These give non-dimensional amplitude and frequency as $A^* = A_1/D = 0.6$, $f^* = f_1/f_N = 0.6$, which is close to that in [Govardhan and Williamson \(2000\)](#).

[Fig. 4](#) is the time history and power spectral density (PSD) of the motion signal under multi-frequency superposition. The PSD of high-frequency components is equal to or greater than the PSD of low-frequency components in velocity and acceleration, even though the displacement amplitude of high-frequency motion is small, which indicates that high-frequency components cannot be neglected.

For multi-frequency motion response, the time-varying coefficients identification problem can be expressed in Eq. (32):

$$\min [F_{real}(t) - F_{Recon}(t)]^2 = [F_{real}(t) - CLe(t)\frac{\rho U^2 DL}{2}\dot{y}(t) - CLa(t)\frac{\pi\rho D^2 L}{4}\ddot{y}(t)]^2. \quad (32)$$

When considering the coupling effect between multiple frequencies, the time-varying excitation coefficient and added-mass coefficient of the mass-spring-dashpot model are obtained using the Forgetting Factor Least Squares method. The force signal reconstructed from time-varying coefficients matches well with the real force, while the constant coefficients CLe CLa obtained through the Least Squares method are not able to accurately reconstruct the real force ([Fig. 5](#)). These results show that the Forgetting Factor Least Squares method proposed in this paper can efficiently identify time-varying parameters when considering the multi-frequency coupling effect. In this case, the excitation coefficient and added-mass coefficient change periodically over time ([Fig. 6](#)), which results from the coupling effect between multiple frequencies. [Fig. 6](#) also shows the PSD of obtained time-varying coefficients considering the coupling effect between ω_1 and ω_2 , where the sum and difference of the coupling frequency, namely, $\omega_1 + \omega_2$, and $\omega_1 - \omega_2$, appear. The results inspire the coupling effect analysis close to the end of Section 3.3.

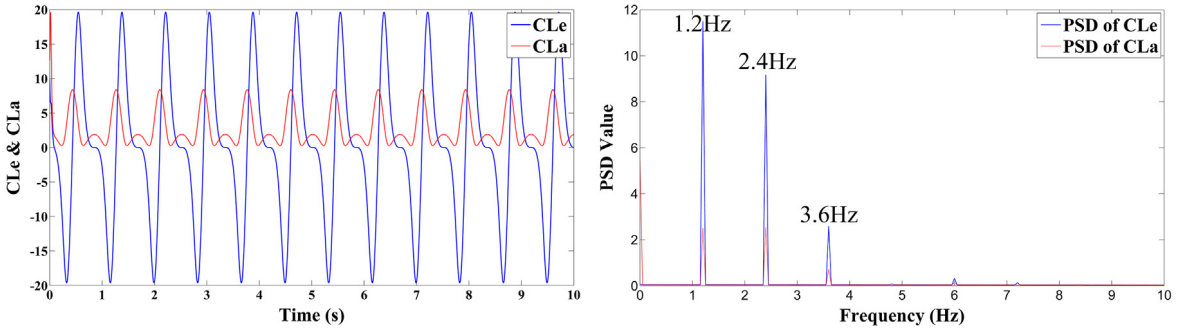


Fig. 6. Time history (left) and power spectrum density (right) of time-varying excitation coefficient and added-mass coefficient considering coupling effect between ω_1 and ω_2 .

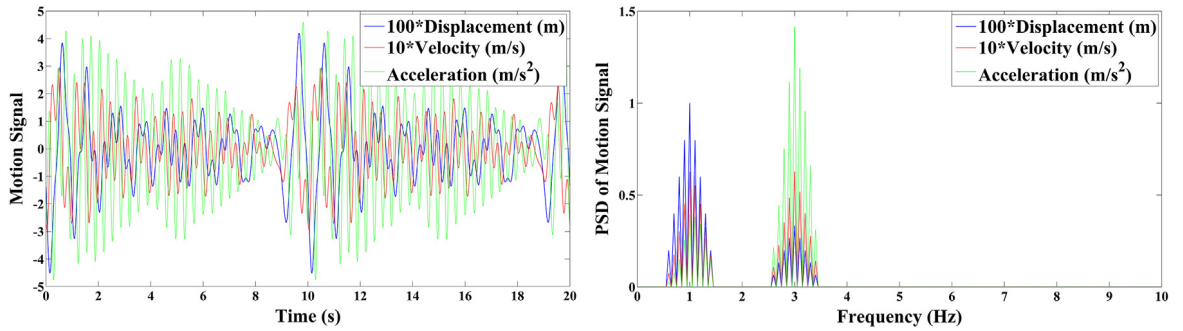


Fig. 7. Time history (left) and power spectrum density (right) of broadband frequency signal (displacement, velocity, and acceleration).

Type 2 motion signals are set as:

$$\left\{ \begin{array}{l} y(t) = \sum_{i=-5}^5 (1 - 0.2^* |i|) A_1 \sin[2\pi(f_1 - 0.1^* i)t + \varphi_{1i}] \\ \quad + \sum_{i=-5}^5 (1 - 0.2^* |i|) A_2 \sin[2\pi(f_2 - 0.1^* i)t + \varphi_{2i}] \\ \dot{y}(t) = \sum_{i=-5}^5 (1 - 0.2^* |i|) 2\pi f_1 A_1 \cos[2\pi(f_1 - 0.1^* i)t + \varphi_{1i}] \\ \quad + \sum_{i=-5}^5 (1 - 0.2^* |i|) 2\pi f_2 A_2 \cos[2\pi(f_2 - 0.1^* i)t + \varphi_{2i}] \\ \ddot{y}(t) = - \sum_{i=-5}^5 (1 - 0.2^* |i|)^2 (2\pi f_1)^2 A_1 \sin[2\pi(f_1 - 0.1^* i)t + \varphi_{1i}] \\ \quad - \sum_{i=-5}^5 (1 - 0.2^* |i|)^2 (2\pi f_2)^2 A_2 \sin[2\pi(f_2 - 0.1^* i)t + \varphi_{2i}] \end{array} \right. \quad (33)$$

where vibration amplitudes $A_1 = 0.01$, $A_2 = 0.01/3$; vibration frequencies $f_1 = 1$ Hz, $f_2 = 3f_1 = 3$ Hz. The non-dimensional amplitude and frequency are $A^* = A_1/D = 0.262$ and $f^* = f_1/f_N = 1$, respectively. Initial phase angles φ_{1i} , φ_{2i} are random numbers between 0 and 2π to avoid periodicity of the signal and potential issues with aliasing and beating effects (Zheng et al., 2014). According to the dynamics of the mass-spring-dashpot system, the force signal $F_{real}(t)$ that causes this motion should satisfy the equation $F_{real}(t) = m\ddot{y}(t) + c\dot{y}(t) + ky(t)$. This force signal is denoted as the real force.

Fig. 7 shows the time history and power spectral density (PSD) of motion superposition of multiple broadband frequencies. This broadband multi-frequency signals provide a better approximation of the chaotic-like signal, as Zheng et al. (2014) observed.

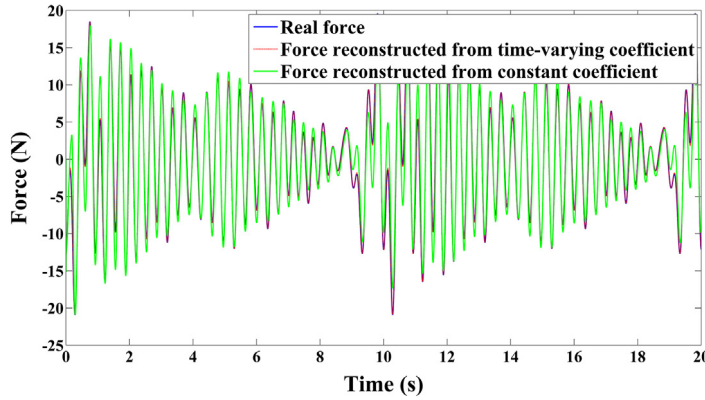


Fig. 8. Comparison of real force, force reconstructed from constant coefficients identified by LS method, and force reconstructed from time-varying coefficients identified by FF-LS method (broadband multi-frequency).

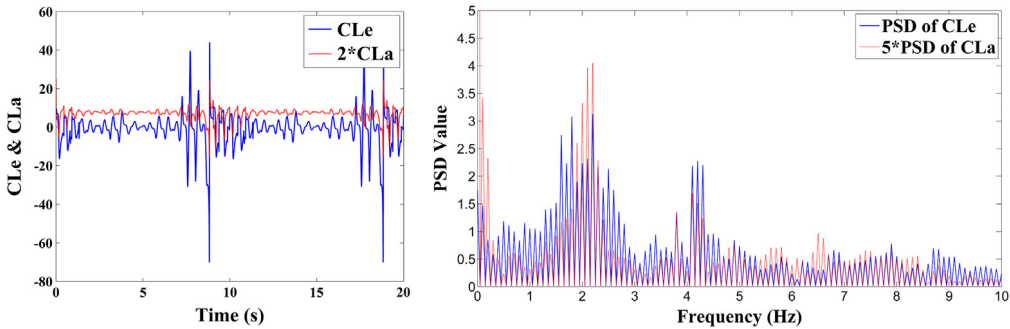


Fig. 9. Time history (left) and power spectrum density (right) of time-varying excitation coefficient and added-mass coefficient considering multi-frequency coupling (broadband multiple frequencies).

Then, the time-varying excitation coefficient and added-mass coefficient of the mass–spring–dashpot model are obtained by the Forgetting Factor Least Squares method proposed in Section 2.1. The force signal reconstructed from time-varying coefficients matches well with the real force, while the constant coefficient obtained through the Least Squares method is not able to reconstruct the real force accurately (Fig. 8). The results show that the Forgetting Factor Least Squares method proposed in this paper can efficiently identify time-varying parameters when considering the broadband multi-frequency coupling effect.

Fig. 9 shows the time history and PSD of the time-varying excitation coefficient and added-mass coefficient under broadband frequency response. In this case, the excitation coefficient and added-mass coefficient are complicated and show chaotic-like characteristics, which is caused by multiple frequency coupling.

3. Time-varying hydrodynamics of a flexible riser under multi-frequency VIV

3.1. Model test

The experiments were performed in the Ocean Engineering Basin at Shanghai Jiao Tong University, where a rotating tower was used to simulate the shear flow. The two ends of the riser were connected to the rotating tower with *universal joints* with a constant pre-tension, which allows the riser model to be simplified as a simple-supported beam model with constant pre-tension. The experimental setup is shown in Fig. 10.

The hydrodynamic diameter of the scaled riser was 31 mm with an effective length of 6.75 m. The slenderness ratio of the riser was 218, and other structural parameters are shown in Table 2.

The structural damping ratio in Table 2 is the structural damping ratio in the air, which was obtained from the free-decay test in air.

In the experiment, Fiber Bragg Grating (FBG) strain gauges were used to measure the strain response of the riser model. The FBG strain sensors are arranged in the CF1, CF2, IL1, and IL2 directions of the riser model and are used to measure the strain in the four directions of the model, namely, ε_{CF1} , ε_{CF2} , ε_{IL1} and ε_{IL2} . A total of 88 Fiber Bragg Grating (FBG) strain sensors were placed on the surface of the riser model in both the CF and IL planes. The locations and arrangements of strain

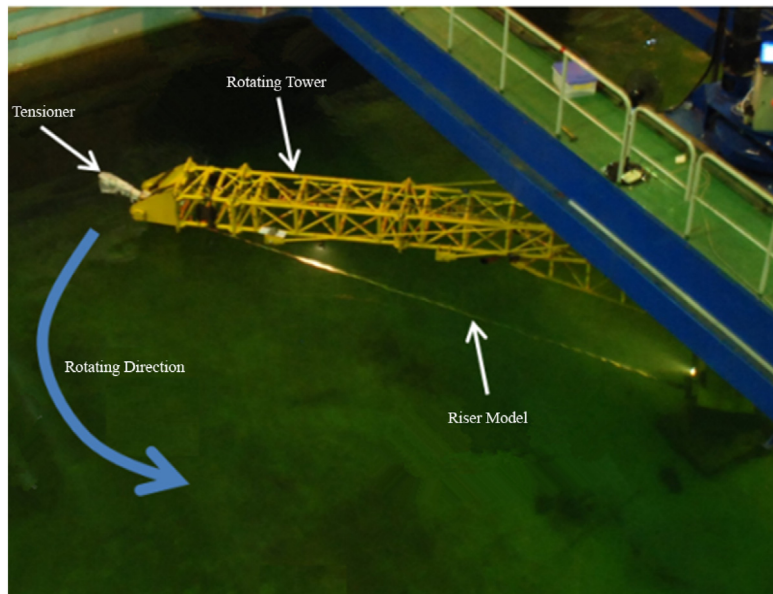


Fig. 10. Testing setup for a flexible riser under shear flow.

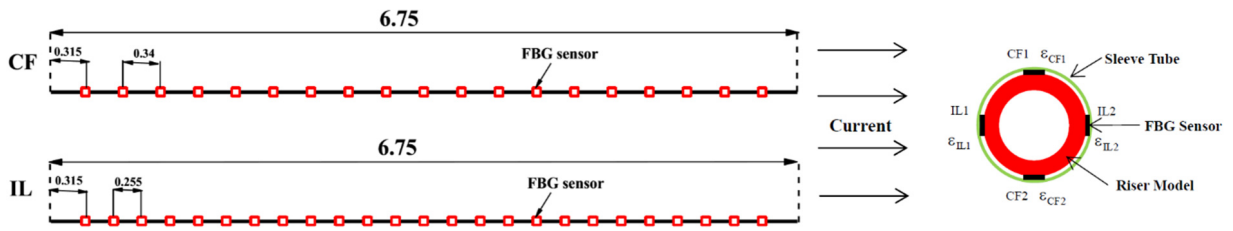


Fig. 11. Locations and arrangements of strain sensors on the surface of the riser model.

Table 2
Riser model parameters.

Parameter	Value	Parameter	Value
Hydrodynamic diameter (m)	0.031	Structural damping ratio (%)	0.3
Diameter (m)	0.03	Axial stiffness (N)	1.45E7
Inner diameter (m)	0.027	Bending stiffness ($N\ m^2$)	1.48E3
Mass per unit length (kg/m)	1.768	Pretension (N)	2943

sensors are shown in Fig. 11. The strain sensor is embedded into the glass fiber with an outer diameter of 125–140 mm, and the fiber was glued to the surface of the riser model. Additionally, a thin sleeved plastic tube covered the outside of the riser model to ensure a smooth surface on the riser. Therefore, FBG strain sensors would not affect the flow around the vibrating riser and the vibration characteristics of the flexible riser. Additionally, strain information of all measuring points in the four directions on the riser model was collected simultaneously, so there is not a phase delay between the measured data at different measuring points.

In this paper, a typical experimental condition; i.e., the vortex-induced vibration response of *CF direction* under 1.5 m/s shear flow (maximum velocity), is analyzed to illustrate the characteristics of time-varying hydrodynamics considering multi-frequency coupling. The relative flow velocity distributions are shown in Fig. 12.

3.2. VIV response and vortex-induced force

A submerged flexible riser with a tensional force in shear flow is illustrated in Fig. 13(a) (Song et al., 2016). The central axis of the riser lies on the Z-axis. The direction of the flow is parallel to the X-Z plane and orthogonal to the riser. The time-invariant mean drag force acts on the riser in the IL plane, which causes a mean deflection in the flow direction of the riser. This deflection is the initial bending, and the corresponding position of the riser is the equilibrium position, as illustrated

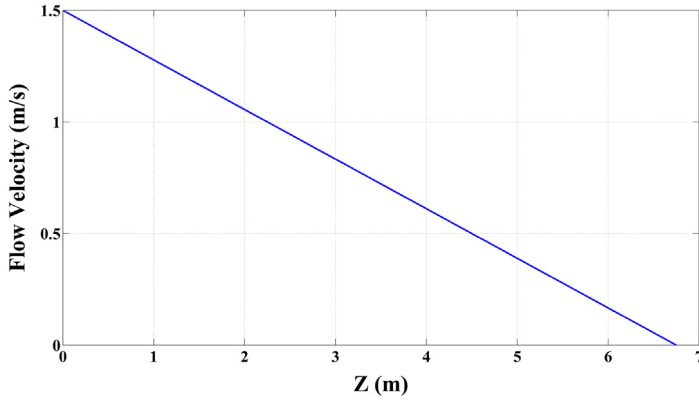


Fig. 12. Flow velocity distributions along axial direction of riser.

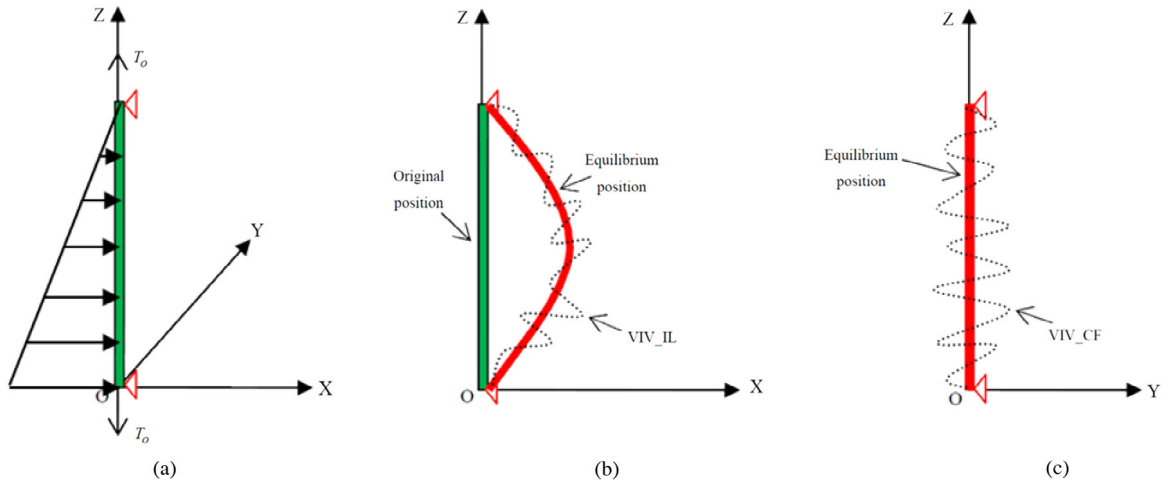


Fig. 13. Response of a submerged flexible riser with a tensional force under uniform flow.

in Fig. 13(b). As fluid flows over the riser, vortices form and are shed periodically. This vortex shedding generates periodic vortex-induced forces in the CF and IL planes with mean values of zero and causes the riser to vibrate in these two planes, which is called vortex-induced vibration (VIV), as illustrated by Fig. 13(b) and (c). Correspondingly, the hydrodynamic forces on the flexible riser also include three parts: vortex-induced forces in both the CF and IL directions and mean drag force in the IL direction.

According to the Finite Element Method (FEM), the governing equation of a spatial beam is:

$$\mathbf{M}\delta'' + \mathbf{C}\delta' + \mathbf{K}\delta = \mathbf{F} \quad (34)$$

where \mathbf{M} , \mathbf{C} and \mathbf{K} are the global mass matrix, damping matrix and stiffness matrix of the riser, respectively; δ , δ' and δ'' are the displacement vector, velocity vector and acceleration vector, respectively and \mathbf{F} is the hydrodynamic force vector. For a riser with N nodes and six degrees of freedom at each node, the dimensions of \mathbf{M} , \mathbf{C} and \mathbf{K} are $6N \times 6N$, and the dimensions of δ and \mathbf{F} are $6N \times 1$.

The stiffness matrix \mathbf{K} of the riser with a tensional force includes two parts:

$$\mathbf{K} = \mathbf{K}_a^e + \mathbf{K}_b^e \quad (35)$$

where \mathbf{K}_a^e is the prestressed stiffness matrix caused by axial tension in the riser, and \mathbf{K}_b^e is the small displacement linear stiffness matrix caused by the riser bending stiffness. Rayleigh damping model gives the damping matrix \mathbf{C} of the riser:

$$\mathbf{C} = \alpha^* \mathbf{M} + \beta^* \mathbf{K} \quad (36)$$

where α and β are the Rayleigh damping coefficients, which can be derived by the natural frequency and structural damping ratio of the riser.

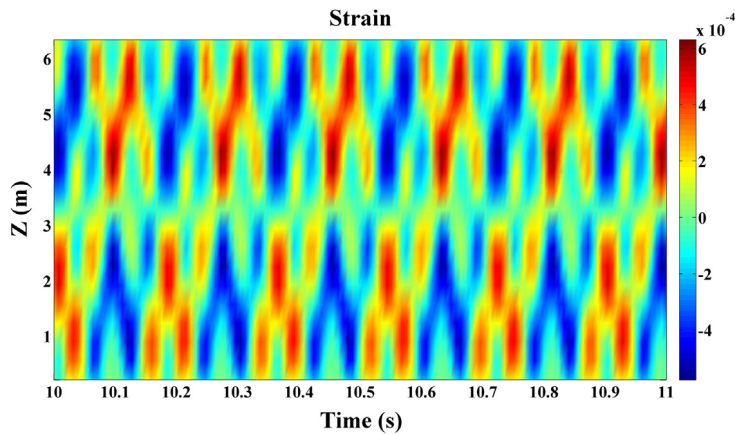


Fig. 14. Time–space distributions of VIV strain.

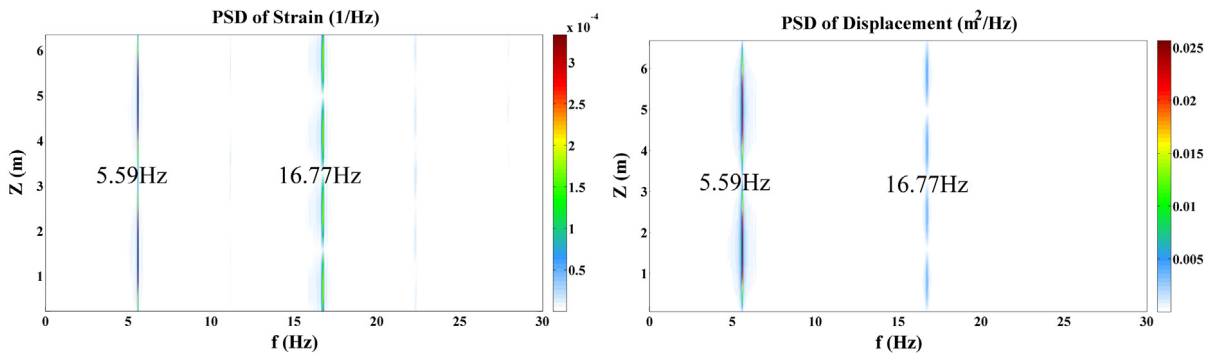


Fig. 15. PSD distributions of VIV strain (left) and VIV displacement (right).

The displacement vector δ of the riser can be expressed as:

$$\delta = [\delta_1, \delta_2, \dots, \delta_N]^T \quad (i = 1 \sim N) \quad (37)$$

where N is the node number. δ_i is the displacement vector of the riser at node i :

$$\delta_i = [z_i \ x_i \ y_i \ \theta_{zi} \ \theta_{yi} \ \theta_{xi}]^T \quad (38)$$

where z_i is the axial displacement at node i ; x_i and y_i are the bending displacements in the IL and CF directions at node i , respectively. θ_{zi} is the torsion angle of the riser at node i around the riser axis; namely, the Z-axis. θ_{yi} and θ_{xi} are the angular displacements at node i around the Y-axis and X-axis, which are induced by the vibration in the IL and CF directions, respectively. Tension variation caused by axial elongation is relatively small compared to pretension (2943N), and universal joints are used at the two ends of the riser to constrain any twisting. Thus, in the following hydrodynamic forces analysis, the impact of axial elongation and torsion is neglected; namely, $z_i = 0$ and $\theta_{zi} = 0$.

The axial tensile displacement of the riser can be calculated from the tensile strain of the riser surface; the bending displacement in the IL and CF directions can be obtained from the bending strain of the standpipe surface using modal analysis (Hu et al., 2012, 2010; Lie and Kaasen, 2006). Appendix B shows the preprocessing of bending strain and modal analysis to obtain VIV displacements of the riser in the CF and IL directions.

With displacement vector δ , the velocity vector δ' and acceleration vector δ'' are obtained by using the central-difference method to calculate the first-order and second-order time derivatives of δ .

After obtaining the structural response vectors δ , δ' and δ'' , with the mass matrix M , the stiffness matrix K and damping matrix C , the inverse analysis gives the hydrodynamic force F on the right side of Eq. (34). The hydrodynamic force F obtained through the inverse analysis method contains a six-degree-of-freedom force (force in the X, Y, Z directions and moment about the X, Y, Z axis). In the following analysis, we focus on the hydrodynamic force in the CF direction (Y-direction) and denote the hydrodynamic force F components obtained in the CF direction as 'real force'.

Fig. 14 is the time–space distributions of VIV strain. Fig. 15 shows the Power Spectral Density (PSD) distributions of VIV strain and VIV displacement. The results show that VIV strain in the CF direction contains multiple frequency

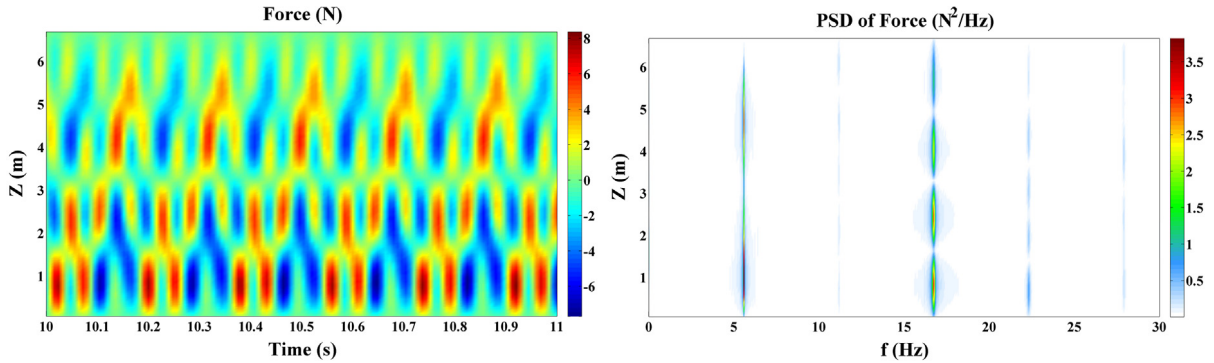


Fig. 16. Time-space distributions (left) and PSD distributions (right) of vortex-induced force.

components. The frequency with the maximum power spectral density of the VIV strain is the basic frequency $\omega_1 = 2\pi^*f_1 = 2\pi^*5.59$ rad/s. At the same time, the high-frequency (three times of the basic frequency) response also appears and is denoted as $\omega_2 = 2\pi^*f_2 = 2\pi^*16.77$ rad/s.

The VIV displacements reconstructed from modal analysis also contain multiple frequency components (Fig. 15). The vortex-induced force of the riser is reconstructed from VIV response (displacement, velocity, and acceleration) by inverse finite element theory. Obtained vortex-induced force in the CF direction is used as ‘real force’ to verify the correctness of the hydrodynamics identification results. Fig. 16 shows the time-space distributions of the vortex-induced force, time history of the vortex-induced force at the midpoint of the riser, and PSD distributions of vortex-induced force, respectively. The results show that high-frequency vortex-induced forces at three times the basic frequency $3\omega_1$ also appears. Dahl et al. (2010) also found vortex-induced forces at three times the basic frequency in the two-dimensional free vibration test of a rigid cylinder. PSD distributions of the vortex-induced force (Fig. 16) also indicate that high-frequency components cannot be neglected.

In the following, we apply the method developed in Section 2 on the VIV response and vortex-induced force obtained in this part.

3.3. Time-varying vortex-induced force coefficients

First, the vortex-induced force, VIV velocity and VIV acceleration are decomposed into components at the basic frequency $\omega_1 = 2\pi^*5.59$ rad/s and high frequency $\omega_2 = 2\pi^*16.77$ rad/s through bandpass filtering. Filter bandwidths are 5 Hz–6 Hz and 16–17 Hz. These components are denoted as $f_{CF}(z, t, \omega_1)$, $f_{CF}(z, t, \omega_2)$, $\dot{y}(z, t, \omega_1)$, $\dot{y}(z, t, \omega_2)$, $\ddot{y}(z, t, \omega_1)$, $\ddot{y}(z, t, \omega_2)$ in the following description.

The linear superposition of VIV response at the basic frequency and high frequency is shown below. Vortex-induced force is also processed in the same way; namely:

$$\begin{cases} y_{multi}(z, t) = y(z, t, \omega_1) + y(z, t, \omega_2) \\ \dot{y}_{multi}(z, t) = \dot{y}(z, t, \omega_1) + \dot{y}(z, t, \omega_2) \\ \ddot{y}_{multi}(z, t) = \ddot{y}(z, t, \omega_1) + \ddot{y}(z, t, \omega_2) \\ f_{multi}(z, t) = f_{CF}(z, t, \omega_1) + f_{CF}(z, t, \omega_2). \end{cases} \quad (39)$$

Fig. 17 shows the time-space distributions of vortex-induced force superposition under basic frequency ω_1 and high-frequency ω_2 . Compared with the time-space distributions of vortex-induced force before filtering in Fig. 16, we find that force superposition under basic frequency ω_1 and high frequency ω_2 can represent major characteristics of real vortex-induced force. Fig. 18 shows the time history comparison among forces before filtering, force at the basic frequency ω_1 , forces at high frequency ω_2 and force superposition under basic frequency ω_1 and high frequency ω_2 . It is obvious that forces at the basic frequency or forces at high frequency could not represent the force before filtering, while force superposition under basic frequency ω_1 and high frequency ω_2 are close enough to the real force before filtering. Fig. 19 compares the axial distributions of the RMS value, and similar results can be concluded. The real force $f_{CF}(z, t)$ obtained through inverse analysis is approximated as $f_{multi}(z, t)$, which is used in the following coupling effect analysis in that its frequency components are known. Velocity and acceleration are processed in the same way.

Substituting $f_{CF}(z, t, \omega_1)$, $\dot{y}(z, t, \omega_1)$, $\ddot{y}(z, t, \omega_1)$ into Eq. (10), vortex-induced force coefficients at basic frequency ω_1 can be obtained according to:

$$f_{CF}(z, t, \omega_1) = \frac{\rho D I U^2(z, t)}{2\sqrt{2}\text{RMS}(\dot{y}(z, t, \omega_1))} CLe(z, \omega_1) \dot{y}(z, t, \omega_1) - \frac{\rho \pi D^2 l}{4} CLa(z, \omega_1) \ddot{y}(z, t, \omega_1). \quad (40)$$

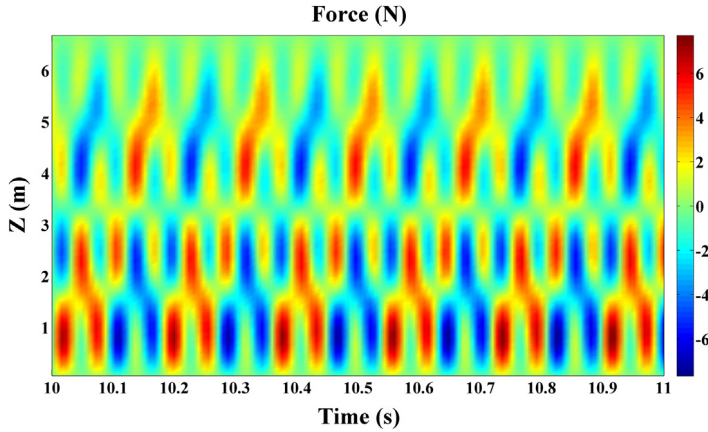


Fig. 17. Time-space distributions of vortex-induced force superposition under basic frequency ω_1 and high frequency ω_2 .

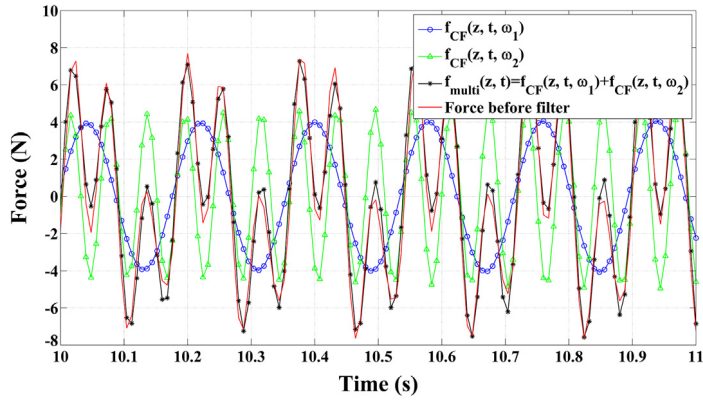


Fig. 18. Time history of vortex-induced force at $z = 0.81$ m (the blue hollow circle: force at basic frequency ω_1 , the green triangle: force at high-frequency ω_2 , the black star: force superposition of basic frequency ω_1 and high-frequency ω_2 , the red line: before filter).

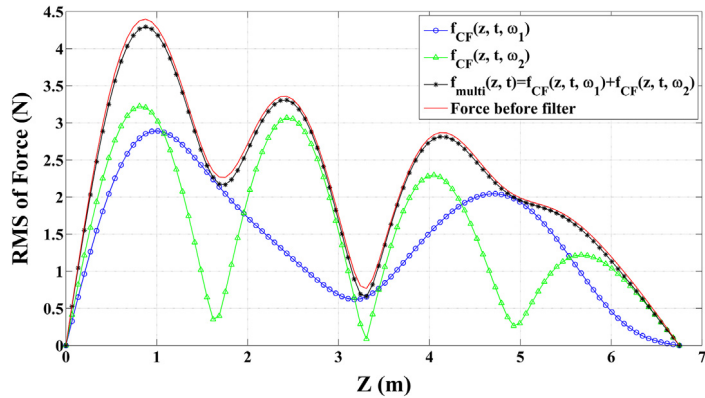


Fig. 19. Axial distributions of RMS value of vortex-induced force (the blue hollow circle: force at basic frequency ω_1 , the green triangle: force at high frequency ω_2 , the black star: force superposition of basic frequency ω_1 and high frequency ω_2 , the red line: before filter).

We can also obtain the vortex-induced force coefficients at the high frequency ω_2 in a similar way. They are used for comparison with time-varying vortex-induced force coefficient under coupling between the basic frequency ω_1 and the high frequency ω_2 .

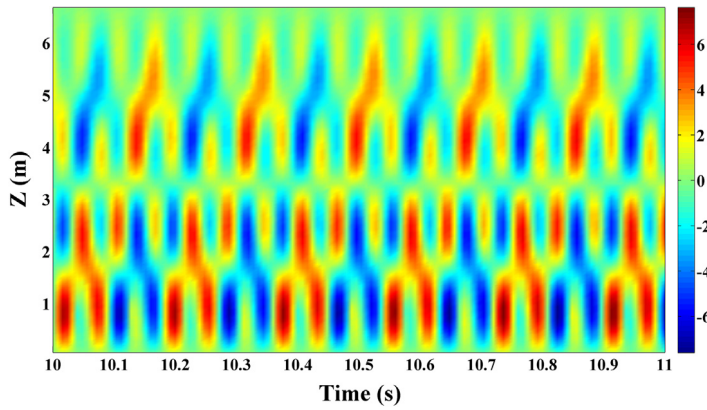


Fig. 20. Time–space distributions of force reconstructed from time-varying vortex-induced force coefficients identified from FF-LS method under coupling of multiple frequencies ($z = 0.81$ m).

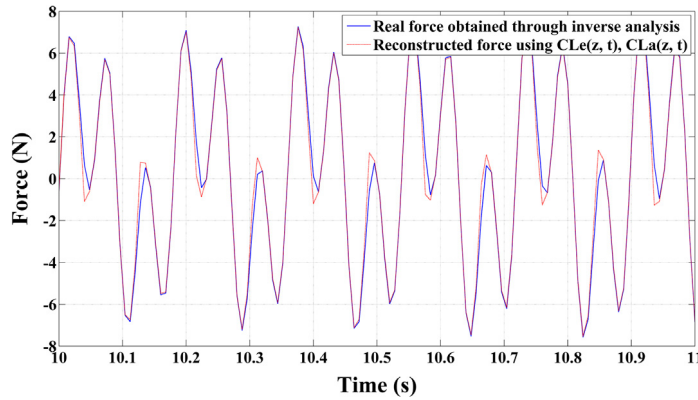


Fig. 21. Comparison between real vortex-induced force and force reconstructed from time-varying vortex-induced force coefficients identified by FF-LS method ($z = 0.81$ m).

Substituting Eq. (39) into the time-varying vortex-induced force model in Eq. (11), we obtain the following equation of the vortex-induced force coefficients $CLe(z, t)$, $CLa(z, t)$:

$$f_{multi}(z, t) = \frac{\rho D l U^2(z, t)}{2\sqrt{2}RMS(\dot{y}_{multi}(z, t))} CLe(z, t) \dot{y}_{multi}(z, t) - \frac{\rho \pi D^2 l}{4} CLa(z, t) \ddot{y}_{multi}(z, t). \quad (41)$$

Then time-varying vortex-induced force coefficients are identified by using the Forgetting Factor Least Squares method. Namely, for any moment t_L , substituting time history of $f_{multi}(z, t)$ at node z from the initial moment t_1 to the present moment t_L as \mathbf{f}_L and time history of $\dot{y}(z, t)$, $\ddot{y}(z, t)$ from the initial moment t_1 to the present moment t_L as \mathbf{H}_L in Eq. (17), we can get $\theta(L)$ from Eq. (27), which gives $CLe(z, t)$, $CLa(z, t)$ at t_L moment at location z after normalization.

To verify the correctness of the identified time-varying vortex-induced force coefficients $CLe(z, t)$, $CLa(z, t)$, the obtained coefficients are used to reconstruct the vortex-induced force as below:

$$f_{Recon}(z, t) = \frac{\rho D l U^2(z, t)}{2\sqrt{2}RMS(\dot{y}_{multi}(z, t))} CLe(z, t) \dot{y}_{multi}(z, t) - \frac{\rho \pi D^2 l}{4} CLa(z, t) \ddot{y}_{multi}(z, t). \quad (42)$$

The definition of $\dot{y}_{multi}(z, t)$, $\ddot{y}_{multi}(z, t)$ is shown in Eq. (39).

The time–space distributions of the reconstructed force are shown in Fig. 20, which is consistent with the real force (Fig. 17). Fig. 21 compares the time history of the reconstructed force and real force where $z = 0.81$ m, and they are in agreement. These results indicate time-varying vortex-induced force coefficients identified by the FF-LS method can reproduce major distribution characteristics of vortex-induced force.

Figs. 22 and 23 are time–space distributions and time histories of the excitation coefficient and added-mass coefficient under multi-frequency coupling where $z = 0.81$ m. They are also compared with coefficients under the basic frequency and high frequency at the same point, which do not change over time. These figures show that the excitation coefficient and added-mass coefficient change periodically over time and contains multiple frequency components.

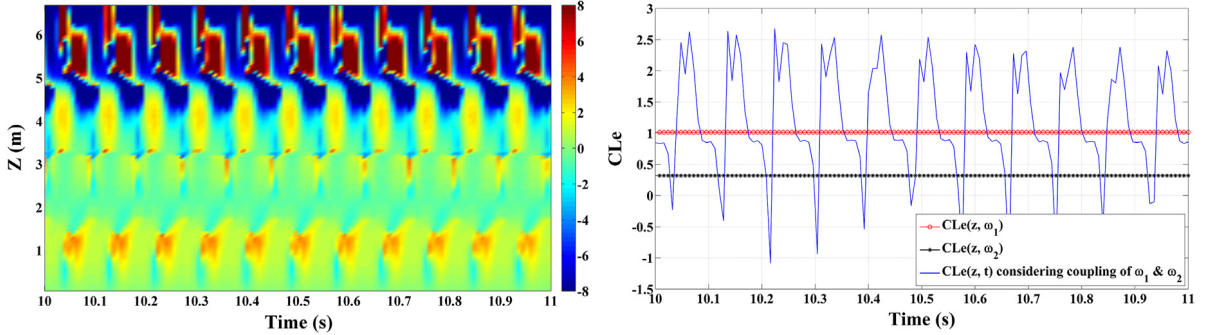


Fig. 22. Time–space distributions (left) and time history (right, $z = 0.81$) of excitation coefficients under coupling between basic frequency ω_1 and high-frequency ω_2 .

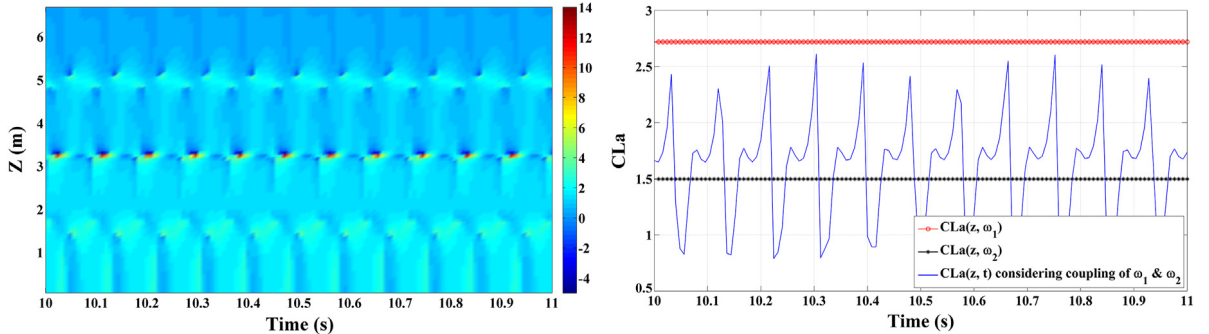


Fig. 23. Time–space distributions (left) and time history (right, $z = 0.81$) of added-mass coefficients under coupling between basic frequency ω_1 and high-frequency ω_2 .

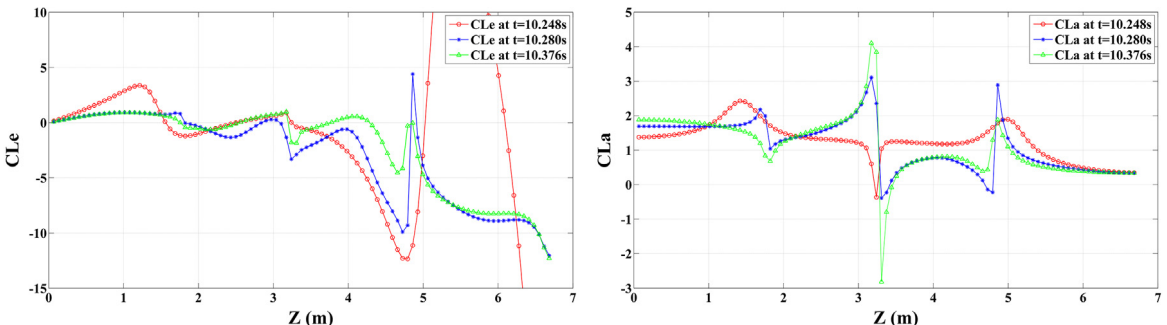


Fig. 24. Axial distributions of excitation coefficients (left) and added-mass coefficients (right) at different moments under coupling between basic frequency ω_1 and high frequency ω_2 (the red hollow circle: $t = 10.248$ s, the blue star: $t = 10.280$ s, the green triangle: $t = 10.376$ s).

Fig. 24 is axial distributions of the excitation coefficient and added-mass coefficient at several different moments. For time-varying effects under coupling of multi-frequency, the axial distributions of vortex-induced force coefficients vary significantly at different moments. The relatively large value of excitation coefficients near the right ends of the riser comes from the normalization term $\frac{\rho D U^2(z,t)}{2\sqrt{2} \dot{y}_{RMS}(z)}$ for excitation coefficients. The shear flow velocity near the right ends of the flexible riser is relatively small (e.g. $U(z, t) = 0.222$ m/s at $z = 5.75$), which gives a large normalization factor. Wu et al. (2008) and Larsen et al. (2016) also have relatively large coefficients at the place where background flow velocity is small. To interpret the ‘sudden jump’ appearing in the axial distribution of added-mass coefficients, we show the axial distribution of the multi-frequency acceleration and vortex-induced force at $t = 10.376$ s in Fig. 25. As the location varies from $z = 3$ m to the ‘sudden jump’ region ($3.25 < z < 3.45$ m), the acceleration varies from positive to negative, while the vortex-induced force is always a negative sign. The sign change of acceleration results in the sign reversal; i.e. ‘sudden jump’ of the added-mass coefficients at $t = 10.376$ s from 4 to -3. One probable explanation for the sign reversal location difference between

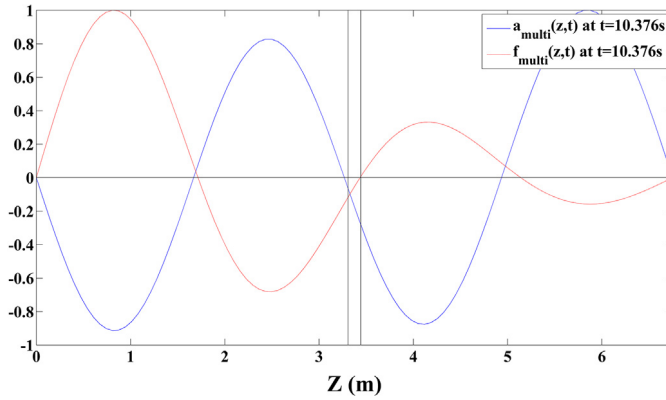


Fig. 25. Axial distribution of the acceleration and vortex-induced force at $t = 10.376$ s.

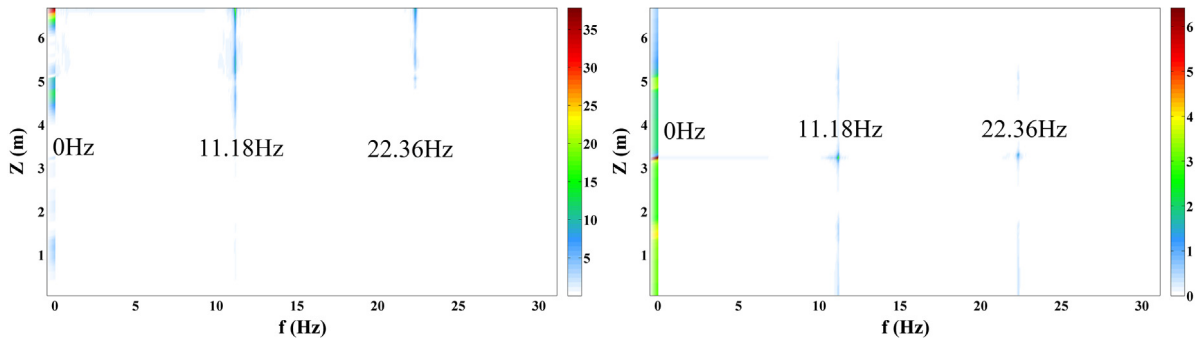


Fig. 26. PSD distributions of time-varying excitation coefficients (left) and added-mass coefficients (right) under coupling between basic frequency ω_1 and high frequency ω_2 .

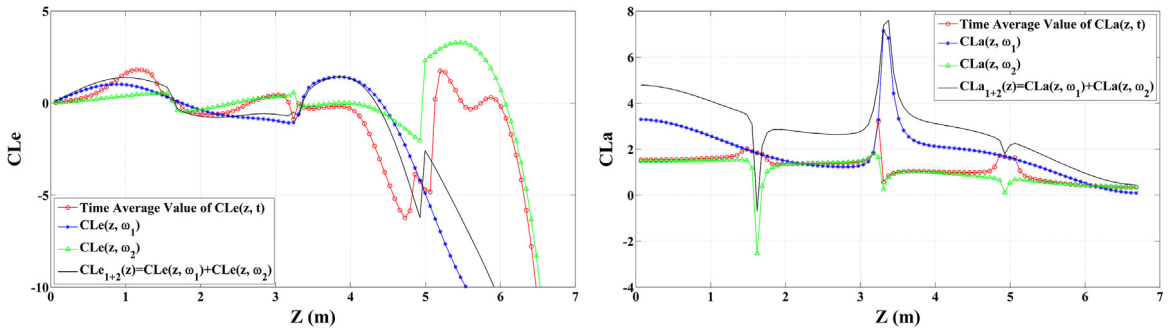


Fig. 27. Axial distributions of excitation coefficients (left) and added-mass coefficients (right) (the red hollow circle: Time-average of time-varying excitation coefficient under coupling between basic frequency ω_1 and high frequency ω_2 , the blue star: basic frequency ω_1 , the green triangle: high frequency ω_2 , the black line: Sum of excitation coefficient at basic frequency ω_1 and high frequency ω_2).

acceleration and vortex-induced force is the multi-mode response characteristics of flexible riser under vortex-induced vibration.

To investigate the vibration components of identified time-varying coefficients, we perform a Fourier analysis for the time-varying coefficients considering multi-frequency coupling. Fig. 26 shows Power Spectrum Density distributions of time-varying vortex-induced force coefficients. Aside from steady components that do not change over time (0 Hz components demonstrated in PSD distributions), vibration components appear in time-varying coefficients whose frequencies are 11.18 Hz and 22.36 Hz. It should be noted that these two frequencies are the difference and sum of the high frequency and basic frequency, respectively ($\omega_2 - \omega_1 = 2\pi * 11.18$ rad/s, $\omega_2 + \omega_1 = 2\pi * 22.36$ rad/s).

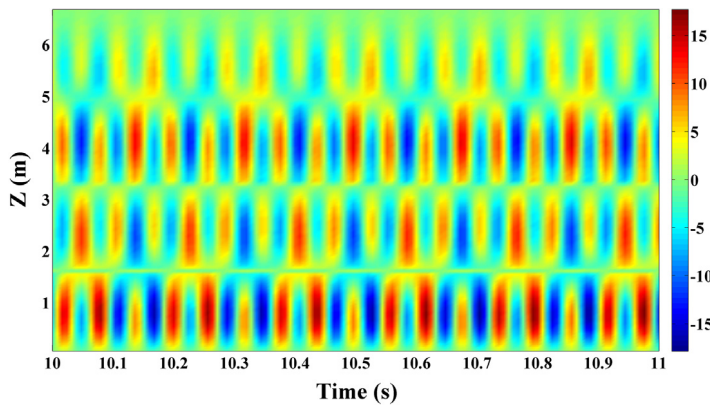


Fig. 28. Time–space distributions of vortex-induced force reconstructed from superposition of vortex-induced force coefficients of basic frequency ω_1 and high frequency ω_2 ($z = 0.81$ m).

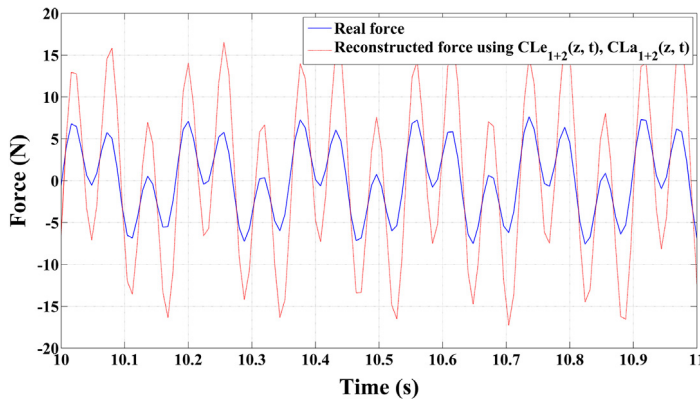


Fig. 29. Comparison between real vortex-induced force and force reconstructed from sum of vortex-induced force coefficients of basic frequency ω_1 and high frequency ω_2 ($z = 0.81$ m).

To explain the appearance of these two vibration components, we assume time-varying coefficients $CLe(z, t)$, $CLa(z, t)$ are the sum of different frequency components; namely:

$$CLe(z, t) = \sum_i CLe(z, t, \omega_i), CLa(z, t) = \sum_i CLa(z, t, \omega_i). \quad (43)$$

In the equation above, $CLe(z, t, \omega_i)$, $CLa(z, t, \omega_i)$ are vibration components at different frequencies of time-varying coefficients under multi-frequency coupling, while $CLe(z, \omega_i)$, $CLa(z, \omega_i)$ in Eq. (10) are steady coefficients for vortex-induced force and the response containing a specific frequency component. Substituting Eqs. (43), (40) into Eq. (42), it becomes:

$$\begin{aligned} f_{CF}(z, t, \omega_1) + f_{CF}(z, t, \omega_2) &= \frac{\rho D l U^2(z, t)}{2\sqrt{2} RMS(\dot{y}_{multi}(z))} \left[\sum_i CLe(z, t, \omega_i) \right] [\dot{y}(z, t, \omega_1) + \dot{y}(z, t, \omega_2)] \\ &\quad - \frac{\rho \pi D^2 l}{4} \left[\sum_i CLa(z, t, \omega_i) \right] [\ddot{y}(z, t, \omega_1) + \ddot{y}(z, t, \omega_2)], \quad i = 1, 2, 3, \dots \end{aligned} \quad (44)$$

Expanding the right-side of Eq. (44) and using formulas for trigonometric functions:

$$\begin{cases} \sin \omega_1 t \cos \omega_2 t = [\sin(\omega_1 + \omega_2)t + \sin(\omega_1 - \omega_2)t]/2 \\ \cos \omega_1 t \sin \omega_2 t = [\sin(\omega_1 + \omega_2)t - \sin(\omega_1 - \omega_2)t]/2 \\ \cos \omega_1 t \cos \omega_2 t = [\cos(\omega_1 + \omega_2)t + \cos(\omega_1 - \omega_2)t]/2 \\ \sin \omega_1 t \sin \omega_2 t = [\cos(\omega_1 + \omega_2)t - \cos(\omega_1 - \omega_2)t]/2. \end{cases} \quad (45)$$

The left hand of Eq. (44) contains components at ω_1, ω_2 , while the right-side of the above equation contains vibration components at $\omega_i + \omega_1, \omega_i - \omega_1, \omega_i + \omega_2, \omega_i - \omega_2$, $i = 1, 2, 3, \dots$. Considering the orthogonality of the trigonometric function as deduced in Eq. (15), the vibration frequencies of the right-side of Eq. (44) should be equal to the left-side of

Eq. (44), which leads to a possible solution of $\omega_i = 0, 2\omega_1, \omega_2 - \omega_1, \omega_2 + \omega_1, 2\omega_2$. This comparison explains the steady components and vibration components at the sum of coupled frequencies and the difference of coupled frequencies for identified time-varying coefficients qualitatively.

Fig. 27 shows the axial distributions comparison of the excitation coefficients and added-mass coefficients.

Comparing these results, we find that:

(1) The vortex-induced force coefficient at high frequency has a different distribution mode from that at the basic frequency.

(2) Time-average values of vortex-induced force coefficients under multi-frequency coupling are different from vortex-induced force coefficients at the basic frequency, which results from the coupling effect from high frequency.

To show the advantages of time-varying hydrodynamics, we compare forces reconstructed from time-varying vortex-induced force coefficients with force reconstructed from the sum of vortex-induced force coefficients at the basic frequency and high frequency without coupling, assuming vortex-induced force obtained from the inverse analysis as the real force. The sum of vortex-induced force coefficients at the basic frequency ω_1 and high frequency ω_2 are calculated as follows:

$$\begin{aligned} CLe_{1+2}(z) &= CLe(z, \omega_1) + CLe(z, \omega_2) \\ CLa_{1+2}(z) &= CLa(z, \omega_1) + CLa(z, \omega_2). \end{aligned} \quad (46)$$

Vortex-induced force is reconstructed using the equation below:

$$f_{1+2}(z, t) = \frac{\rho DlU^2(z, t)}{2\sqrt{2}RMS(\dot{y}_{multi}(z))} CLe_{1+2}(z)\dot{y}_{multi}(z, t) - \frac{\rho\pi D^2l}{4} CLa_{1+2}(z)\ddot{y}_{multi}(z, t). \quad (47)$$

Time-space distributions of reconstructed force are shown in **Fig. 28**. We compare the time-space distributions with that of real force obtained from the inverse analysis (**Fig. 16**) and compare time history of reconstructed force with real force at the node $z = 0.81$ m (**Fig. 29**). It is obvious that vortex-induced force obtained by linear superposition of vortex-induced coefficients at multiple frequencies without coupling cannot reflect the distribution characteristics of real force.

To explain this difference, substituting Eqs. (16), (39) and (46) into Eq. (47), the reconstructed force through the sum of coefficients at multiple frequencies can be expressed as:

$$\begin{aligned} f_{Recon}(z, t) &= \frac{\rho DlU^2(z, t)}{2\sqrt{2}} * \frac{[CLe(z, \omega_1) + CLe(z, \omega_2)] * [\dot{y}(z, t, \omega_1) + \dot{y}(z, t, \omega_2)]}{\sqrt{y_{RMS}(z, \omega_1)^2 + y_{RMS}(z, \omega_2)^2}} \\ &\quad - \frac{\rho\pi D^2l}{4} [CLa(z, \omega_1) + CLa(z, \omega_2)] * [\ddot{y}(z, t, \omega_1) + \ddot{y}(z, t, \omega_2)] \\ &= \frac{\rho DlU^2(z, t)}{2\sqrt{2}} * \left[\frac{CLe(z, \omega_1)\dot{y}(z, t, \omega_1) + CLe(z, \omega_2)\dot{y}(z, t, \omega_2)}{\sqrt{y_{RMS}(z, \omega_1)^2 + y_{RMS}(z, \omega_2)^2}} \right. \\ &\quad \left. + \frac{CLe(z, \omega_1)\dot{y}(z, t, \omega_2) + CLe(z, \omega_2)\dot{y}(z, t, \omega_1)}{\sqrt{y_{RMS}(z, \omega_1)^2 + y_{RMS}(z, \omega_2)^2}} \right] \\ &\quad - \frac{\rho\pi D^2l}{4} [CLa(z, \omega_1)\ddot{y}(z, t, \omega_1) + CLa(z, \omega_2)\ddot{y}(z, t, \omega_2)] \\ &\quad + CLa(z, \omega_1)\ddot{y}(z, t, \omega_2) + CLa(z, \omega_2)\ddot{y}(z, t, \omega_1)]. \end{aligned} \quad (48)$$

Substituting Eq. (39) into $f_{multi}(z, t) = f_{CF}(z, t, \omega_1) + f_{CF}(z, t, \omega_2)$, it is expressed as:

$$\begin{aligned} f_{multi}(z, t) &= f_{CF}(z, t, \omega_1) + f_{CF}(z, t, \omega_2) \\ &= \frac{\rho DlU^2(z, t)}{2\sqrt{2}} \left[\frac{CLe(z, \omega_1)\dot{y}(z, t, \omega_1)}{\dot{y}_{RMS}(z, \omega_1)} + \frac{CLe(z, \omega_2)\dot{y}(z, t, \omega_2)}{\dot{y}_{RMS}(z, \omega_2)} \right] \\ &\quad - \frac{\rho\pi D^2l}{4} [CLa(z, \omega_1)\ddot{y}(z, t, \omega_1) + CLa(z, \omega_2)\ddot{y}(z, t, \omega_2)]. \end{aligned} \quad (49)$$

Comparing Eq. (49) with (48), the cross-terms $\frac{CLe(z, \omega_1)\dot{y}(z, t, \omega_2) + CLe(z, \omega_2)\dot{y}(z, t, \omega_1)}{\sqrt{y_{RMS}(z, \omega_1)^2 + y_{RMS}(z, \omega_2)^2}}$ and $CLa(z, \omega_1)\ddot{y}(z, t, \omega_2) + CLa(z, \omega_2)\ddot{y}(z, t, \omega_1)$ in Eq. (48) contribute significantly to the difference between real vortex-induced force and force reconstructed from vortex-induced force coefficients superposition of basic frequency ω_1 and high frequency ω_2 . The difference between using $\sqrt{y_{RMS}(z, \omega_1)^2 + y_{RMS}(z, \omega_2)^2}$ and using $\dot{y}_{RMS}(z, \omega_1), \dot{y}_{RMS}(z, \omega_2)$ separately to normalize the excitation coefficient also contribute to this difference.

From the above analysis, the cross term produced when using the sum of coefficients under basic frequency ω_1 and high frequency ω_2 overestimates the vortex-induced force when reconstructing it. This comparison shows the advantages of time-varying vortex-induced force coefficients considering multi-frequency coupling, which can reconstruct vortex-induced force accurately.

Aside from reconstructing the vortex-induced force, we will use the time-space distribution of obtained added-mass coefficients to predict the natural frequency and response displacement. The governing equation of a tensioned beam with

time-space varying added-mass coefficients is:

$$\frac{\partial^2}{\partial z^2} [EI \frac{\partial^2 w(z, t)}{\partial z^2}] - T \frac{\partial^2 w(z, t)}{\partial z^2} + [m + m_{added}(z, t)] \frac{\partial^2 w(z, t)}{\partial t^2} = F(z, t) \quad (50)$$

where $w(z, t)$ is the lateral vibration displacement, EI is the bending stiffness, T is the constant pretension, m is the mass per unit length and $m_{added}(z, t)$ is the added-mass per unit length; i.e. $Cla(z, t) \frac{\pi D^2 \rho}{4}$. In natural frequency and response calculations, we assume external force $F(z, t)$ as zero.

The energy method is performed to approximate natural frequency. Assuming the harmonic vibration for the j th order vibration, or $w_j(z, t) = \varphi_j(z) \sin(\omega_j t + \beta)$, then the maximum kinetic energy and the maximum potential energy can be expressed as:

$$\begin{aligned} T_{\max} &= \frac{1}{2} \omega_j^2 \int_0^L [m + m_{added}(z, t)] (\varphi_j(z))^2 dz \\ V_{\max} &= \frac{1}{2} \int_0^L EI \left(\frac{d^2 \varphi_j(z)}{dz^2} \right)^2 dz + \frac{1}{2} \int_0^L T \left(\frac{d \varphi_j(z)}{dz} \right)^2 dz. \end{aligned} \quad (51)$$

In that maximum kinetic energy should equal the maximum potential energy, it gives the j th order natural frequency in the form of the Rayleigh quotient (Bokaian, 1990):

$$\omega_j^2(t) = R(\varphi_j) = \frac{\frac{1}{2} \int_0^L EI \left(\frac{d^2 \varphi_j(z)}{dz^2} \right)^2 dz + \frac{1}{2} \int_0^L T \left(\frac{d \varphi_j(z)}{dz} \right)^2 dz}{\int_0^L [m + m_{added}(z, t)] (\varphi_j(z))^2 dz}. \quad (52)$$

The problem is finding a function $\varphi_j(z)$ that minimizes the above Rayleigh quotient so that the corresponding $\omega_j(t)$ is the natural frequency. To make a finite-dimensional approximation of this variational problem, we express the continuous function $\varphi_j(z)$ as $\varphi_j(z) = \sum_{i=1}^n A_{ji} \psi_i(z)$, where $\psi_i(z)$, $i = 1, 2, \dots, n$ are the orthogonal functions that satisfy the boundary condition. Considering the boundary condition of this simply supported beam (shown in Fig. 13), we choose $\psi_i(z) = \sin(\frac{iz}{L})$. Therefore, we obtain the necessary condition for minimizing the Rayleigh quotient, which is:

$$\frac{\partial R}{\partial A_i} (i = 1, 2, \dots, n). \quad (53)$$

It ends up as a generalized eigenvalue problem:

$$(\mathbf{K}_a - \omega_j^2(t)) \mathbf{A}_j = \mathbf{0}, j = 1, 2, \dots, n. \quad (54)$$

The elements of \mathbf{K}_a , \mathbf{M}_a are $[\mathbf{K}_a]_{st} = \int_0^L EI \psi_s''(z) \psi_t''(z) dz + \int_0^L T \psi_s'(z) \psi_t'(z) dz$ and $[\mathbf{M}_a]_{st} = \int_0^L [m + m_{added}(z, t)] \psi_s(z) \psi_t(z) dz$. Solving this eigenvalue problem at each time step will render the time-varying natural frequencies. For obtained natural frequencies $\omega_j(t)$, the corresponding eigenvectors \mathbf{A}_j will give the vibration displacement amplitude distributions according to $\varphi_j(z) = \sum_{i=1}^n A_{ji} \psi_i(z)$.

If the added-mass coefficients are chosen as a constant, i.e. $m_{added}(z, t) = 1$, \mathbf{K}_a , \mathbf{M}_a both become diagonal matrices, and the eigenvector \mathbf{A}_j , $j = 1, 2, \dots, n$ become unit vectors and thus, $\varphi_j(z)$, $j = 1, 2, \dots, n$ become sinusoidal functions. Also, the natural frequencies have theoretical solutions:

$$f_{ni} = \frac{i}{2L} \sqrt{\frac{(\pi i)^2 EI}{L^2(m + m_{added})} + \frac{T}{m + m_{added}}}, i = 1, 2, \dots, n. \quad (55)$$

Fig. 30 compares the second and fourth order natural frequency calculated through the above framework with time-space varying added-mass coefficients, natural frequency with added-mass coefficient “1”, and experimental response frequency. It reveals that the fourth order frequencies (the blue solid line) calculated with time-space varying added-mass coefficients are close to the high order response frequency observed from experiments (the red dashed line). In contrast, the fourth order natural frequency calculated by “1” added-mass coefficient is different from the high order response frequency observed in experiments. Fig. 31 compares the RMS value of displacements (normalized by its maximum value over z) predicted by time-space varying coefficients with experimental data. It shows that time-space varying added-mass coefficients can predict the displacement amplitude distribution better than “1” added-mass coefficients for high order response. The probable explanation is that the variation of added-mass coefficients from “1” (potential flow added-mass coefficient for the cylinder) results in the modification of flexible’s natural frequency to match certain vortex-shedding frequency.

From these two figures, the time-space varying added-mass coefficients show some difference when predicting basic frequency response. This difference results from two probable reasons. Initially, the energy method posted here is a finite-dimensional approximation for the continuous beam system. This approximation is equivalent to adding the constraints on the beam system which increase the natural frequency from theoretical results. Secondly, in the current analysis, we do not consider the time-space varying excitation coefficients. The effect of excitation coefficients is equivalent to external force in Eq. (50), i.e. $F(z, t) = CLe(z, t) \frac{\rho D U^2(z, t)}{2\sqrt{2} \text{RMS}(\dot{w}(z, t))} \frac{\partial w(z, t)}{\partial t}$, which will also modify the structural natural frequency and the modal shape. Trying to take time-space varying excitation coefficients into account and investigate the effect on the flexible riser response is the direction of our future work.

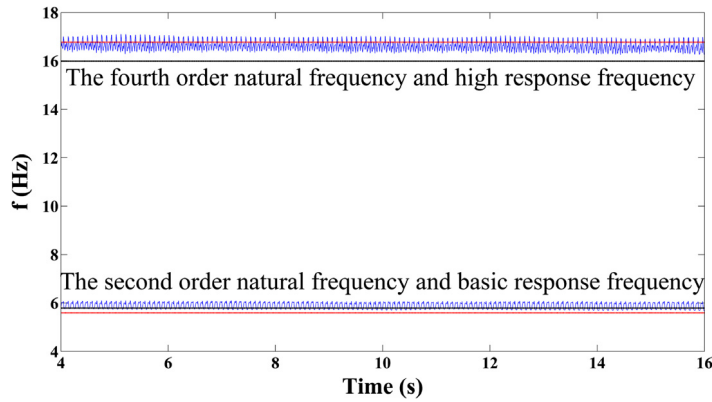


Fig. 30. The second and fourth order natural frequencies predicted from time–space varying added-mass coefficients (the blue solid line), natural frequency calculated with “1” added-mass coefficient (the black dashed line), and response frequency from experimental data (the red dashed line).

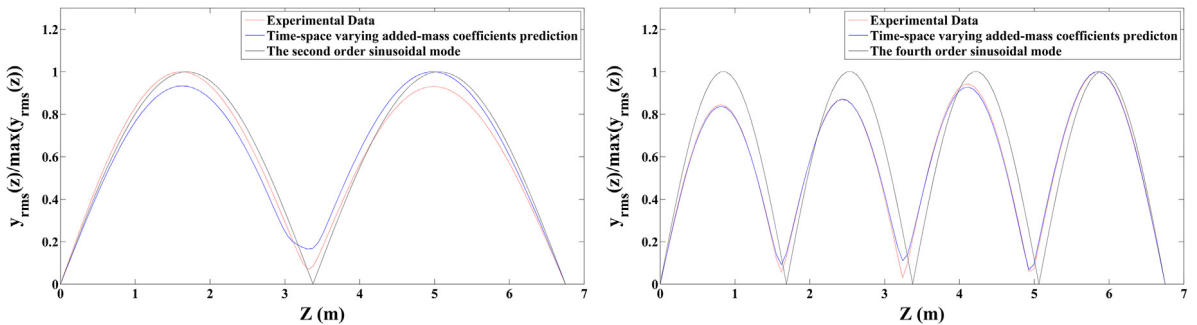


Fig. 31. RMS value of the second order (left) and fourth order (right) displacements predicted from time–space varying added-mass coefficients (the blue solid line), from experimental data (the red dashed line) and predicted with “1” added-mass coefficient (the black dashed line).

4. Conclusion

This paper proposes the Forgetting Factor Least Squares Method (FF-LS) for identification of time-varying hydrodynamics of a flexible riser under multi-frequency vortex-induced vibrations (VIV). By following this procedure for all sampled data of a flexible riser undergoing multi-frequency VIV, the corresponding time-varying hydrodynamics in the Cross-Flow (CF) direction considering multi-frequency coupling are obtained. The results show that, under multi-frequency coupling, vortex-induced force coefficients of the flexible risers change periodically and are different from the coefficients at the basic frequency usually used in VIV prediction. For time-varying effects under coupling of the basic frequency and high frequency, the axial distributions of vortex-induced force coefficients vary significantly at different moments. Time-varying coefficients considering multi-frequency coupling contain steady components and vibration components whose frequencies are the sum of coupling frequencies and the difference of coupling frequencies. This phenomenon is explained qualitatively from orthogonality of trigonometric function. This paper compares the forces reconstructed from different vortex-induced force coefficients, assuming vortex-induced force obtained from the inverse analysis as the real force. The results reveal that time-varying vortex-induced force coefficients considering the coupling effect between multiple frequencies can reconstruct vortex-induced force accurately, while the sum of vortex-induced force coefficients under multiple frequencies produces the cross term that overestimates the vortex-induced force.

Acknowledgments

This research was supported by the National Natural Science Foundation of China under Grant Number 51490674 and 51490675.

Appendix A. Validation for single frequency VIV response of flexible riser

In Section 2.2, proposed FF-LS method is validated when applied to *multiple frequency* signals. In this appendix, it shows that when applied to the *single frequency* VIV, it will give same results as previously published paper (Song et al., 2016).

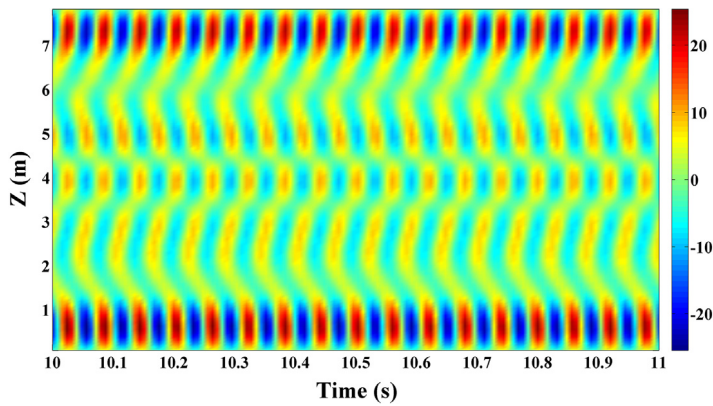


Fig. 32. Time–space distributions of vortex-induced force at basic frequency ω_1 .

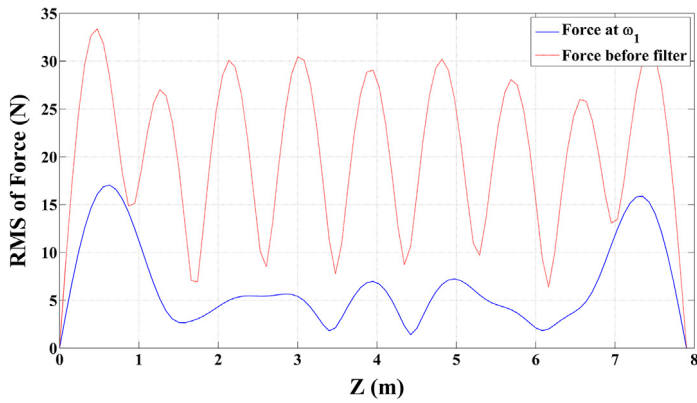


Fig. 33. Axial distributions of RMS value of vortex-induced force (the red dotted line: before filter, the blue solid line: basic frequency ω_1).

Identified vortex-induced force coefficients of the flexible riser under the *single frequency* is obtained to verify the correctness of this method (results of a 7.9 m length flexible riser under 2.8 m/s uniform flow). Vortex-induced force is determined from measured VIV response through the inverse analysis method. Afterwards, vortex-induced force $f_{CF}(z, t, \omega_1)$, velocity $\dot{y}(z, t, \omega_1)$ and acceleration $\ddot{y}(z, t, \omega_1)$ at the basic frequency are obtained through a bandpass filter (in this verification case, $\omega_1 = 16.8$ Hz, and the filtering bandwidth is 15.5–17.5 Hz). Fig. 32 shows the time–space distribution of vortex-induced force at the single frequency, and Fig. 33 compares the axial distribution of vortex-induced force at a single frequency ω_1 with force before filter.

Based on Eq. (10), the vortex-induced force under single frequency can be decomposed as:

$$f_{CF}(z, t, \omega_i) = \frac{\rho D l U^2(z, t)}{2\sqrt{2}y_{RMS}(z, \omega_i)} CLe(z, \omega_i) \dot{y}(z, t, \omega_i) - \frac{\rho \pi D^2 l}{4} CLa(z, \omega_i) \ddot{y}(z, t, \omega_i) \quad i = 1, 2. \quad (56)$$

Forgetting Factor Least Square method is used to identify vortex-induced force coefficients at the basic frequency. Fig. 34 shows that identified vortex-induced force coefficients at the basic frequency do not change over time. Fig. 35 compares the single frequency force $f_{CF}(z, t, \omega_1)$ obtained through a band-pass filter with reconstructed force using coefficients obtained through FF-LS method proposed in this paper. The result shows that the FF-LS method proposed is applicable for single frequency VIV response as well as vortex-induced force.

In Figs. 36 and 37, the results showed that vortex-induced force coefficients are consistent with those obtained by Song et al. (2016), which further verifies the correctness of the proposed method.

Appendix B. Bending strain and bending displacement

The axial tension of the riser model will change periodically when the riser undergoes vortex-induced vibration. The strain $\varepsilon_{CF1}(z, t)$ and $\varepsilon_{CF2}(z, t)$ measured by FBG strain sensor in the CF direction will include two parts: tensile strain caused

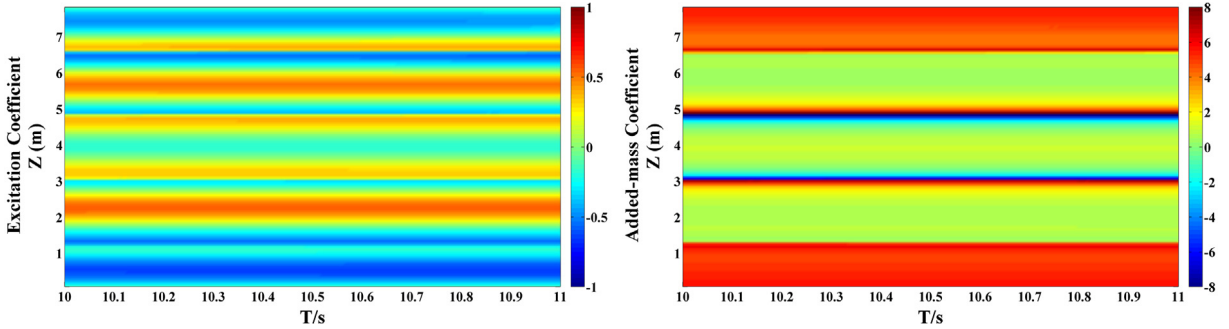


Fig. 34. Time–space distributions of excitation coefficient (left) and added-mass coefficient (right) at basic frequency ω_1 obtained by Forgetting Factor Least Squares method.

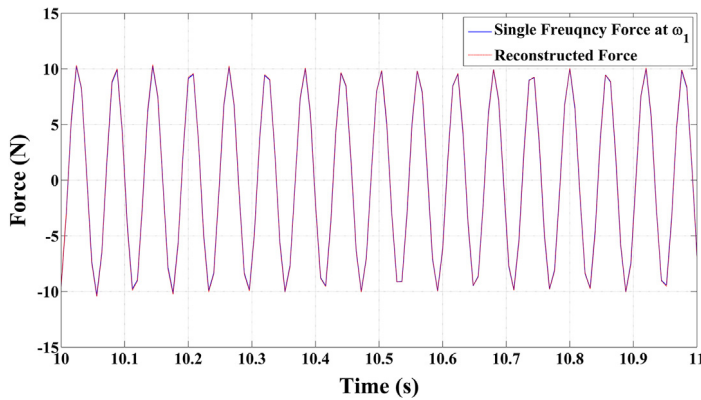


Fig. 35. Comparison between real vortex-induced force and force reconstructed from identified vortex-induced force coefficients (basic frequency ω_1).

by axial tension $\varepsilon_{CF-T}(z, t)$ and bending strain $\varepsilon_{CF}(z, t)$ generated by VIV:

$$\begin{aligned}\varepsilon_{CF1}(z, t) &= \varepsilon_{CF-T}(z, t) + \varepsilon_{CF}(z, t) \\ \varepsilon_{CF2}(z, t) &= \varepsilon_{CF-T}(z, t) - \varepsilon_{CF}(z, t).\end{aligned}\quad (57)$$

Transforming the above equation, then the bending strain $\varepsilon_{CF}(z, t)$ in the CF direction caused by VIV is:

$$\varepsilon_{CF}(z, t) = [\varepsilon_{CF1}(z, t) - \varepsilon_{CF2}(z, t)] / 2. \quad (58)$$

When the bending strain of the riser is obtained, the bending displacement of the riser can be obtained by modal analysis. For example, the VIV displacement time history of the riser at node z $y(z, t)$ can be expressed as:

$$y(z, t) = \sum_{i=h}^k p_i(t) \varphi_i(z), \quad z \in [0, L] \quad (59)$$

where $\varphi_i(z)$ is the i th displacement mode of the riser in the local coordinate system, and $p_i(t)$ is time history of displacement weight.

Both the bending displacement $y(z, t)$ and the bending strain $\varepsilon(z, t)$ satisfy the equation below:

$$\frac{\partial^2 y(z, t)}{\partial z^2} = -\frac{\varepsilon(z, t)}{R}. \quad (60)$$

From Eqs. (59) and (60), the bending strain $\varepsilon(z, t)$ can be obtained:

$$\varepsilon(z, t) = -R \sum_{i=h}^k p_i(t) \varphi_i''(z). \quad (61)$$

Therefore, when the bending strain $\varepsilon_{CF}(z, t)$ of the riser in CF direction is obtained from Eq. (58), time history of displacement mode weight $p_i(t)$ can be obtained according to Eq. (61). Then the bending displacement response $y(z, t)$ of the riser in CF direction can be obtained by Eq. (59).

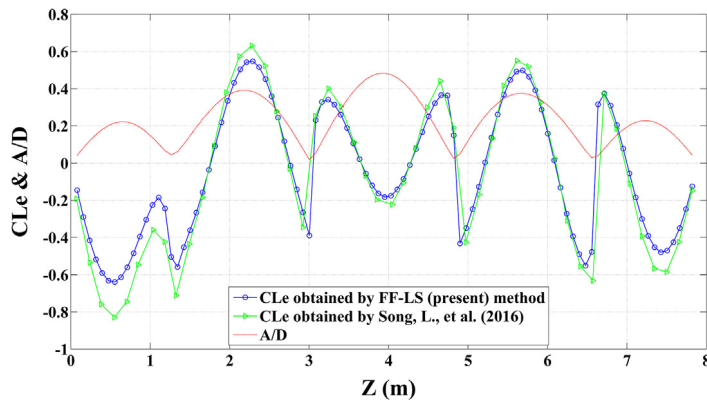


Fig. 36. Axial distributions of excitation coefficient and amplitude ratio at basic frequency ω_1 (the blue hollow round: CLe obtained by FF-LS, the green triangle: CLe obtained by Song et al. (2016), the red dashed line: amplitude ratio at the basic frequency ω_1).

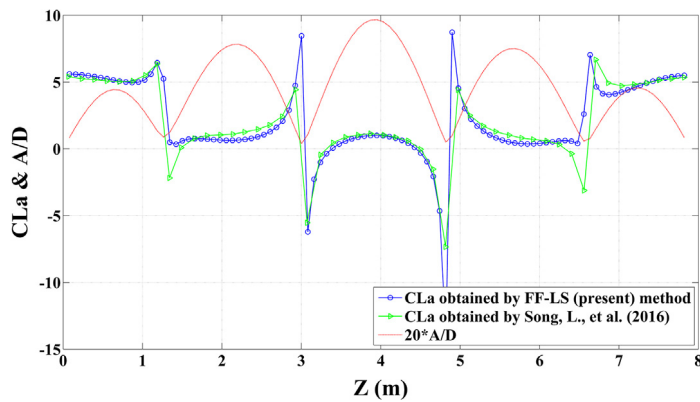


Fig. 37. Axial distributions of added-mass coefficient and amplitude ratio at basic frequency ω_1 (the blue hollow round: CLa obtained by FF-LS, the green triangle: CLa obtained by Song et al. (2016), the red dashed line: amplitude ratio at the basic frequency ω_1).

Appendix C. Abbreviation and nomenclature

Abbreviation	
FF-LS	Forgetting Factor Least Squares method
VIV	Vortex-induced Vibration
CF	Cross-Flow
IL	In-Line
RMS	Root Mean Square value
FBG	Fiber Bragg Grating
FEM	Finite Element Method
PSD	Power Spectral Density
2T	Vortex shedding modes where a triplet of vortices is formed in each half cycle

Nomenclature	
z	The axial position of a flexible riser
t	Time
ω_i	The i th response frequency $i = 1, 2, \dots$
ω_1	The basic response frequency $\omega_1 = 2\pi f_1 = 2\pi * 5.59 \text{ rad/s}$
ω_2	The high order response frequency $\omega_2 = 2\pi f_2 = 2\pi * 16.77 \text{ rad/s}$
φ_i	The initial phase angle at the frequency ω_i , $i = 1, 2, \dots$
θ_i	The initial phase difference between force at ω_i and VIV displacement at ω_i , $i = 1, 2, \dots$
$y(z, t)$	Displacement time history in CF direction of the riser at node z

(continued on next page)

(continued)

$y(z, t, \omega_i)$	Displacement time history at position z in CF direction at one single vibration frequency ω_i , $i = 1, 2, \dots$
$y_0(z, \omega_i)$	Amplitude of displacement at position z in CF direction at one single vibration frequency ω_i , $i = 1, 2, \dots$
$\dot{y}(z, t)$	Velocity time history in CF direction of the riser at node z
$\ddot{y}(z, t, \omega_i)$	Velocity time history at position z in CF direction at one single vibration frequency ω_i , $i = 1, 2, \dots$
$\ddot{y}(z, t)$	Acceleration time history in CF direction of the riser at node z
$\ddot{y}(z, t, \omega_i)$	Acceleration time history at position z in CF direction at one single vibration frequency ω_i , $i = 1, 2, \dots$
$x(z, t)$	Displacement time history in IL direction of the riser at node z
$x_0(z)$	The time average bending displacement in IL direction
$x(z, t, \omega_i)$	The displacement time history at position z in IL direction at one single vibration frequency ω_i , $i = 1, 2, \dots$
$f_{CF}(z, t)$	The time history of vortex-induced force in CF direction at node z
$f_{CF}(z, t, \omega_i)$	Time history of vortex-induced force at position z in CF direction at frequency ω_i , $i = 1, 2, \dots$
$f_0(z, \omega_i)$	The amplitude of vortex-induced force at position z in CF direction at frequency ω_i
$\dot{y}(z, t, \omega_1)$	Velocity time history at position z in CF direction at one single vibration frequency ω_1
$\dot{y}(z, t, \omega_2)$	Velocity time history at position z in CF direction at one single vibration frequency ω_2
$\ddot{y}(z, t, \omega_1)$	Acceleration time history at position z in CF direction at one single vibration frequency ω_1
$\ddot{y}(z, t, \omega_2)$	Acceleration time history at position z in CF direction at one single vibration frequency ω_2
$y_{multi}(z, t)$	$y_{multi}(z, t) = y(z, t, \omega_1) + y(z, t, \omega_2)$
$\dot{y}_{multi}(z, t)$	$\dot{y}_{multi}(z, t) = \dot{y}(z, t, \omega_1) + \dot{y}(z, t, \omega_2)$
$\ddot{y}_{multi}(z, t)$	$\ddot{y}_{multi}(z, t) = \ddot{y}(z, t, \omega_1) + \ddot{y}(z, t, \omega_2)$
$f_{multi}(z, t)$	$f_{multi}(z, t) = f_{CF}(z, t, \omega_1) + f_{CF}(z, t, \omega_2)$
$f_{Recon}(z, t)$	Reconstructed force time history at position z using identified time-varying hydrodynamic coefficients $CLe(z, t)$ and $CLa(z, t)$
$f_{1+2}(z, t)$	Reconstructed force time history at position z using superposition of hydrodynamic coefficients at the basic frequency and high frequency: $CLe_{1+2}(z) CLa_{1+2}(z)$
l	Element unit length
$CLe(z, \omega_i)$	The excitation coefficient at the node z at frequency ω_i
$CLa(z, \omega_i)$	The added-mass coefficient at the node z at frequency ω_i
$CLe(z, t)$	Time history of excitation coefficient at position z considering multi-frequency coupling
$CLa(z, t)$	Time history of the added-mass coefficient at position z considering multi-frequency coupling
$CLe(z, t, \omega_i)$	ω_i frequency component of $CLe(z, t)$
$CLa(z, t, \omega_i)$	ω_i frequency component of $CLa(z, t)$
$CLe_{1+2}(z)$	$CLe_{1+2}(z) = CLe(z, \omega_1) + CLe(z, \omega_2)$
$CLa_{1+2}(z)$	$CLa_{1+2}(z) = CLa(z, \omega_1) + CLa(z, \omega_2)$
$RMS(*)$	Root Mean Square value of time history of variable *
$\dot{y}_{RMS}(z)$	$\dot{y}_{RMS}(z) = RMS(y(z, t))$
$\dot{y}_{RMS}(z, \omega_i)$	$\dot{y}_{RMS}(z, \omega_i) = RMS(y(z, t, \omega_i))$
ρ	Fluid density
$U(z, t)$	Flow velocity relative to the riser (VIV velocity of the riser is not considered) at the position z at t moment
D	The hydrodynamic diameter of the riser.
\mathbf{f}_L	$\mathbf{f}_L = [f_{CF}(z, t_1), f_{CF}(z, t_2), f_{CF}(z, t_3), \dots, f_{CF}(z, t_L)]^T$, $L = 1, 2, 3, \dots$
t_1	the time history vortex-induced force at node z from initial moment t_1 to present moment t_L
\mathbf{H}_L	$\mathbf{H}_L = [\mathbf{h}(1), \mathbf{h}(2), \mathbf{h}(3), \dots, \mathbf{h}(L)]^T$ $= \begin{bmatrix} \dot{y}(z, t_1), \dot{y}(z, t_2), \dot{y}(z, t_3), \dots, \dot{y}(z, t_L) \\ \ddot{y}(z, t_1), \ddot{y}(z, t_2), \ddot{y}(z, t_3), \dots, \ddot{y}(z, t_L) \end{bmatrix}^T$, $L = 1, 2, 3, \dots$
$\theta(L)$	the time history of velocity and acceleration at node z from initial moment t_1 to present moment t_L $\theta(L) = \begin{bmatrix} \frac{\rho D U^2}{2\sqrt{2}\dot{y}_{RMS}(z)} CLe(z, t_L) \\ \frac{\rho\pi D^2}{4} CLa(z, t_L) \end{bmatrix}$, $L = 1, 2, 3, \dots$
t_1	$\theta(L)$ is dimensional vortex-induced force coefficient at node z at moment t_L .
t_L	The initial moment
$t_1, t_2, t_3, \dots, t_L$	The present moment
$t_1, t_2, t_3, \dots, t_L$	sampling time (totally L groups of data is sampled)

(continued)

β	Decaying factor, $0 < \beta \leq 1$
μ	Forgetting factor, $\mu = \beta^2$
\mathbf{f}_L^*	$\mathbf{f}_L^* = [\beta^{L-1}\mathbf{f}_L(1), \beta^{L-2}\mathbf{f}_L(2), \dots, \beta\mathbf{f}_L(L-1), \mathbf{f}_L(1)]^T$ weighted time history vortex-induced force at node z from the initial moment t_1 to the present moment t_L
\mathbf{H}_L^*	$\mathbf{H}_L^* = [\beta^{L-1}\mathbf{h}^T(1), \beta^{L-2}\mathbf{h}^T(2), \dots, \beta\mathbf{h}^T(L-1), \mathbf{h}^T(L)]^T$ weighted time history of velocity and acceleration at node from the initial moment t_1 to the present moment t_L
$J(\theta(L))$	$\min J(\theta) = (\mathbf{f}_L^* - \mathbf{H}_L^*\theta)^T(\mathbf{f}_L^* - \mathbf{H}_L^*\theta)$ sum squared error between $\mathbf{H}_L^*\theta(L)$ and \mathbf{f}_L^*
$\hat{\theta}(L)$	$J(\theta(L)) _{\theta(L)=\hat{\theta}(L)} = \min$ value that let $J(\theta(L))$ reaches the minimum
A_L	Weighted matrix, whose diagonal elements are $A(L) = 1$, $A(k-1) = \mu A(k)$, non-diagonal elements is 0
\mathbf{M}	Global mass matrix
\mathbf{C}	Global damping matrix
\mathbf{K}	Global stiffness matrix
δ	Displacement vector
δ'	Velocity vector
δ''	Acceleration vector
\mathbf{F}	Hydrodynamic force vector.
K_a^e	Stiffness matrix caused by axial tension of the riser
K_b^e	Small displacement linear stiffness matrix caused by riser bending stiffness
α, β	Rayleigh damping coefficient
Z_i	Axial displacement at the i th node
x_i	Bending displacements at the i th node in IL direction
y_i	Bending displacements at the i th node in CF direction
θ_{zi}	Torsion angle of riser around Z-axis at the i th node
θ_{yi}	Angular displacement of riser around Y-axis at the i th node
θ_{xi}	Angular displacement of riser around X-axis at the i th node

Nomenclature in Section 2.2 for mass–spring–dashpot system

$y(t), \dot{y}(t), \ddot{y}(t)$	Generated motion signal for the mass–spring–dashpot system (displacement, velocity, and acceleration)
M, C, K	Mass, damping of the dashpot and stiffness of spring
$F_{real}(t)$	Generated force signal according to the dynamics of mass–spring–dashpot system or obtained from rigid cylinder test
$CLe(t)$	Excitation coefficient time history of the rigid cylinder or the mass–spring–dashpot system
$CLA(t)$	Added-mass coefficient time history of the rigid cylinder or the mass–spring–dashpot system
$F_{Recon}(t)$	Reconstructed force time history of the mass–spring–dashpot system
$\omega_1 = 2\pi f_1$	ω_1 is the basic frequency for the mass–spring–dashpot system
$\omega_2 = 2\pi f_2$	ω_2 is the high order frequency for the mass–spring–dashpot system
A_1	The amplitude of the basic frequency vibration
A_2	The amplitude of the high frequency vibration
φ_1	Initial phase angle for the basic frequency vibration, set as zero
φ_2	Initial phase angle for the high frequency vibration, set as zero
φ_{1i}	Random initial phase angle for the broadband frequency vibration
φ_{2i}	Random initial phase angle for the broadband frequency vibration

References

- Bokaian, A., 1990. Natural frequencies of beams under tensile axial loads. *J. Sound Vib.* 142 (3), 481–498.
- Chavent, G., 1979. Identification of distributed parameter systems: about the output least square method, its implementation and identifiability. In: Paper presented at the Proc. 5th IFAC Symposium on Identification and System Parameter Estimation.
- Dahl, J.M., 2008. Vortex-Induced Vibration of a Circular Cylinder with Combined in-Line and Cross-Flow Motion. (Doctoral dissertation), Massachusetts Institute of Technology.
- Dahl, J.M., Hover, F.S., Triantafyllou, M.S., Dong, S., Karniadakis, G.E., 2007. Resonant vibrations of bluff bodies cause multivortex shedding and high frequency forces. *Phys. Rev. Lett.* 99 (14), 144503.
- Dahl, J.M., Hover, F.S., Triantafyllou, M.S., Oakley, O.H., 2010. Dual resonance in vortex-induced vibrations at subcritical and supercritical Reynolds numbers. *J. Fluid Mech.* 643, 395–424.
- Ding, F., Chen, T., 2005. Performance bounds of forgetting factor least-squares algorithms for time-varying systems with finite measurement data. *IEEE Trans. Circuits Syst. I. Regul. Pap.* 52 (3), 555–566.
- Fang, S.M., Niedzwecki, J.M., Fu, S., Li, R., Yang, J., 2014. VIV response of a flexible cylinder with varied coverage by buoyancy elements and helical strakes. *Mar. Struct.* 39, 70–89.
- Gopalkrishnan, R., 1993. Vortex-Induced Forces on Oscillating Bluff Cylinders. Massachusetts Institute of Technology.
- Govardhan, R., Williamson, C.H.K., 2000. Modes of vortex formation and frequency response of a freely vibrating cylinder. *J. Fluid Mech.* 420, 85–130.
- Hu, S.L.J., Bao, X., Li, H., 2010. Model order determination and noise removal for modal parameter estimation. *Mech. Syst. Signal Process.* 24 (6), 1605–1620.
- Hu, S.L.J., Bao, X., Li, H., 2012. Improved polyreference time domain method for modal identification using local or global noise removal techniques. *Sci. China Phys. Mech. Astron.* 55 (8), 1464–1474.

- Hu, S.L.J., Yang, W., Li, H., 2014. A robust high-resolution method for the time-frequency analysis of vortex-induced-vibration signals. *J. Fluids Struct.* 51, 255–280.
- Jauvtis, N., Williamson, C., 2004. The effect of two degrees of freedom on vortex-induced vibration at low mass and damping. *J. Fluid Mech.* 509, 23–62.
- Larsen, C.M., Passano, E., Lie, H., 2016. Recent development of the empirical basis for prediction of vortex induced vibrations. *J. Eng. Technol. Sci.* 48 (1), 111–133.
- Larsen, C.M., Yttervik, R., Aronsen, K., 2007. Calculation of In-Line Vortex Induced Vibrations of Free Spanning Pipelines. In: Paper presented at the ASME 2007 International Conference on Offshore Mechanics and Arctic Engineering.
- Li, L., Fu, S., Xu, Y., Wang, J., Yang, J., 2013. Dynamic responses of floating fish cage in waves and current. *Ocean Eng.* 72 (7), 297–303.
- Li, L., Fu, S., Yang, J., Ren, T., Wang, X., 2011. Experimental investigation on vortex-induced vibration of risers with staggered buoyancy. In: Paper presented at the ASME 2011 30th International Conference on Ocean, Offshore and Arctic Engineering.
- Lie, H., Kaasen, K.E., 2006. Modal analysis of measurements from a large-scale VIV model test of a riser in linearly sheared flow. *J. Fluids Struct.* 22 (22), 557–575.
- Lie, H., Mo, K., Vandiver, J.K., 1998. VIV model test of a bare-and a staggered buoyancy riser in a rotating rig. In: Paper presented at the Offshore Technology Conference.
- Liu, C., Fu, S., Zhang, M., Ren, H., 2017. Time Varying Hydrodynamics Identification of a Flexible Riser Under Multi-Frequency Vortex-Induced Vibrations. In: Paper presented at the ASME 2017 36th International Conference on Ocean, Offshore and Arctic Engineering.
- Marcollo, H., Hinwood, J.B., 2006. On shear flow single mode lock-in with both cross-flow and in-line lock-in mechanisms. *J. Fluids Struct.* 22 (2), 197–211.
- Paleologu, C., Benesty, J., Ciochina, S., 2008. A robust variable forgetting factor recursive least-squares algorithm for system identification. *IEEE Signal Process. Lett.* 15, 597–600.
- Song, L., Fu, S., Cao, J., Ma, L., Wu, J., 2016. An investigation into the hydrodynamics of a flexible riser undergoing vortex-induced vibration. *J. Fluids Struct.* 63, 325–350.
- Sumer, B.M., Fredsøe, J., 2006. Hydrodynamics around cylindrical structures. *Coast. Eng.* 33 (33), 69.
- Trim, A.D., Braaten, H., Lie, H., Tognarelli, M.A., 2005. Experimental investigation of vortex-induced vibration of long marine risers. *J. Fluids Struct.* 21 (3), 335–361.
- Vandiver, J.K., Jaiswal, V., Jhingran, V., 2009. Insights on vortex-induced, traveling waves on long risers. *J. Fluids Struct.* 25 (4), 641–653.
- Vandiver, J.K., Swithenbank, S.B., Jaiswal, V., Jhingran, V., 2006. Fatigue damage from high mode number vortex-induced vibration. In: Paper presented at the 25th International Conference on Offshore Mechanics and Arctic Engineering.
- Wiggins, A.A.D., 2005. Multi-Frequency Cable Vibration Experiments. (Master thesis). Massachusetts Institute of Technology.
- Williamson, C.H.K., Govardhan, R., 2004. Vortex-induced vibrations. *Annu. Rev. Fluid Mech.* 36, 413–455.
- Wu, J., Larsen, C.M., Kaasen, K.E., 2008. A new approach for identification of forces on slender beams subjected to vortex induced vibrations. In: Paper presented at the ASME 2008 27th International Conference on Offshore Mechanics and Arctic Engineering.
- Wu, J., Lie, H., Larsen, C.M., Liapis, S., Baarholm, R., 2016. Vortex-induced vibration of a flexible cylinder: Interaction of the in-line and cross-flow responses. *J. Fluids Struct.* 63, 238–258.
- Zheng, H., Price, R.E., Modarres-Sadeghi, Y., Triantafyllou, M.S., 2014. On fatigue damage of long flexible cylinders due to the higher harmonic force components and chaotic vortex-induced vibrations. *Ocean Eng.* 88, 318–329.